Characterisation of soil deformation over wide strain ranges in triaxial test with high-precision stereophotogrammetry

by

Satoshi Nishimura[1]

[1] Faculty of Engineering, Hokkaido University, Japan

ABSTRACT

Stereophotogrammetry was adopted as means to measure three-dimensional displacements of soil specimen surface in triaxial tests. New developments include an efficient algorithm which resolves the relative displacements with high precision to order of 10^{-3}mm, and strains in common-size soil specimens to order of 10^{-3}%, while correcting for ray refraction effects caused by pressure cell wall and water. The system, requiring only sets of compact-type digital cameras as hardware, allows determining a stiffness-strain curve over wide strain ranges spanning from 10^{-3}% to virtually any large strain with a fixed configuration. This paper explains the proposed image analysis processes, which combines ray tracing formulation by Zhang et al. (2014), Particle Tracking Velocimetry (PTV) and sub-pixel Digital Image Correlation (DIC) in efficiently deriving accurate and precise relative displacements. Rigorous assessment of the accuracy and the precision was conducted. As demonstration, two undrained triaxial compression tests on reconstituted clay were performed with and without end lubrication. Both for small-strain (<0.05%) axial loading-unloading cycles and for monotonic loading to large axial strain (15%), the strain development was tracked and the specimen behaviour was characterised. These tests demonstrate that the new technique can be a useful option in soil laboratory both for research and practice.

INTRODUCTION

Measuring soil deformation characteristics over wide strain ranges is an important part of soil characterisation in many geotechnical projects. Laboratory tests, such as triaxial tests, allow accurate measurement of soil deformation when carefully performed with local displacement transducers. Although strain measurement with local transducers has become an established routine, the involved devices and techniques have not become much less skill-demanding and affordable over the past few decades. The

specimen usually becomes crowded with transducers, which are typically designed exclusively for small-strain measurements, and often interfere with jigs and other parts when large displacements occur. The radial strain measurement in particular is still met with difficulties (Ackerley et al., 2016).

As alternative approach, Nishimura et al. (2016) explored potential use of Digital Image Correlation (DIC) analysis for small-strain investigation in laboratory. The performance of digital cameras in the consumer market has improved dramatically in recent decades, with ever finer resolution and greater image sensor size. For example, Lin and Penumadu (2006) reported an accuracy of 0.2-0.3mm in their digital image analysis. Just 10 years later, Nishimura et al. (2016) report an accuracy and precision in order of 10^{-3}mm, albeit in simpler, one-dimensional conditions. Many researchers took advantage of the development in hardware and computing environment, and image analysis has been adopted for a variety of research topics, from physical model deformation (White et al., 2003), shear strain localisation (Rattez et al., 2021), volume change measurement (Gachet et al., 2007) to liquefaction behaviour (Zhao et al., 2020).

Whilst most of these studies adopted a single camera, and the analysis involves some geometric assumptions between the observed 2D image and the real 3D space, another streak of research explored use of stereophotogrammetry in soil laboratory, which reconstructs three-dimensional coordinates of a point observed as two-dimensional images by multiple cameras. Butterfield et al. (1970) may be amongst the first, followed by more advanced applications (e.g. Desrues and Viggiani, 2004; Qiao et al., 2008). In more recent years, Zhang, Li and co-workers (Zhang et al., 2014, 2019; Li et al., 2016; Li and Zhang, 2018) developed a comprehensive system of stereophotogrammetry for triaxial tests, in which the absolute coordinates of the target in cell water can be determined with an accuracy in order of 10^{-2}mm. While their stated main purpose is to measure the specimen volume (hence the need for accuracy in absolute coordinate measurement), soil deformation characterisation in many circumstances demands a different kind of feature – precision in strain measurement. This is in addition to, or in some case even at expense of, absolute positioning accuracy. This background motivated the author to combine stereophotogrammetry and DIC to achieve the best possible precision in 3D strain measurement.

This paper presents development and validation of the DIC-aided stereophotogrammetric strain measurement method in triaxial tests. What is unique with this study is its effort to resolve displacements and strains to order of 10^{-3}mm and 10^{-3}%. By conceding on absolute positioning accuracy, the set-up is simpler than the above cited works. The application is demonstrated with tests on clay with and without lubricated ends. Attempts were made to derive from images a stiffness-strain curve with as close a quality as to those obtained with modern local transducers. The photogrammetry-based approach has significant merits in laboratory soil testing over the conventional methods with local transducers (very wide trackable deformation ranges, cost-effectiveness and ease of handling with no internal cables, no external amplifiers, etc.) and more specialised techniques such as X-ray tomography (no need for special apparatus design, and no need for loading interruption for scanning). The eventual objective of the work is to demonstrate the value of such merits of the proposed method for geotechnical practice, as well as for research.

BASIC FORMULATION OF STEREOPHOTOGRAMMETRY

Pinhole camera model and camera calibration

The basic theory of stereophotogrammetry is described in many documents (e.g. Raffel et al., 2007; CG-ARTS, 2015; OpenCV website), and a minimum summary is presented below, with occasional reference to implementation. The description assumes using two cameras ('left and 'right'). The theory typically involves a pinhole camera model, as illustrated in Figure 1(a), where the X_w-Y_w-Z_w, X-Y-Z and u-v coordinate systems represent the real physical space (the 'world' coordinates), camera space (with Z as the optical ray axis) and image space in pixels, respectively. The relationship between them is expressed as:

$$\begin{bmatrix} u \\ v \\ 1 \end{bmatrix} = \begin{bmatrix} \frac{f}{\delta_u}\frac{X}{Z} + u_0 \\ \frac{f}{\delta_v}\frac{Y}{Z} + v_0 \\ 1 \end{bmatrix} = \begin{bmatrix} \frac{f}{\delta_u} & 0 & u_0 \\ 0 & \frac{f}{\delta_v} & v_0 \\ 0 & 0 & 1 \end{bmatrix} \begin{bmatrix} X/Z \\ Y/Z \\ 1 \end{bmatrix} = \lambda \begin{bmatrix} \frac{f}{\delta_u} & 0 & u_0 & 0 \\ 0 & \frac{f}{\delta_v} & v_0 & 0 \\ 0 & 0 & 1 & 0 \end{bmatrix} \begin{bmatrix} X \\ Y \\ Z \\ 1 \end{bmatrix} = [\mathbf{A} \quad \mathbf{0}] \begin{bmatrix} X \\ Y \\ Z \\ 1 \end{bmatrix} \tag{1}$$

$$\begin{bmatrix} X \\ Y \\ Z \\ 1 \end{bmatrix} = \begin{bmatrix} r_{11} & r_{12} & r_{13} & t_1 \\ r_{21} & r_{22} & r_{23} & t_2 \\ r_{31} & r_{32} & r_{33} & t_3 \\ 0 & 0 & 0 & 1 \end{bmatrix} \begin{bmatrix} X_w \\ Y_w \\ Z_w \\ 1 \end{bmatrix} = \begin{bmatrix} \mathbf{R} & \mathbf{t} \\ \mathbf{0} & 1 \end{bmatrix} \begin{bmatrix} X_w \\ Y_w \\ Z_w \\ 1 \end{bmatrix} \tag{2}$$

where λ is an arbitrary scalar, f is the focal distance, δ_u and δ_v are the physical spacings between each light-sensing pixel in the u and v directions, respectively, and (u_0, v_0) are the ray axis offsets from the image centre. The above equations are generic, and will be used with superscripts L and R representing left and right cameras, respectively, as shown in Figure 1. The matrix **R** and the vector **t** represent rotation and translation, respectively, between X_w-Y_w-Z_w and X-Y-Z. Any lens distortion such as fish-eye view is to be corrected by modifying **A**. The most common approach is to correct the image by an even-order polynomial function of $r = \sqrt{(fX/Z)^2 + (fY/Z)^2}$ (e.g. Kaehler and Bradski, 2017). Finding very little distortion in the adopted cameras (the coefficient k_1 on r^2 was practically zero), however, the present study did not eventually adopt the correction. From Eqs.(1) and (2),

$$\begin{bmatrix} u \\ v \\ 1 \end{bmatrix} = [\mathbf{A} \quad \mathbf{0}] \begin{bmatrix} \mathbf{R} & \mathbf{t} \\ \mathbf{0} & 1 \end{bmatrix} \begin{bmatrix} X_w \\ Y_w \\ Z_w \\ 1 \end{bmatrix} = [\mathbf{AR} \quad \mathbf{At}] \begin{bmatrix} X_w \\ Y_w \\ Z_w \\ 1 \end{bmatrix} = \mathbf{P} \begin{bmatrix} X_w \\ Y_w \\ Z_w \\ 1 \end{bmatrix} \tag{3}$$

where **P** is the 3x4 perspective projection matrix. As **P** is indeterminate due to the scalar λ, it is obtained in normalised form by fixing p_{34} at 1. When **P** is to be determined from (u, v) vs. (X_w, Y_w, Z_w) correspondence of known calibration points, more than 6 points are required to make the problem overdetermined. The remaining 11 (=3x4 minus 1 corresponding to p_{34}) elements in **P** are then determined by least-square optimisation. The upper triangular matrix **A** and the orthogonal matrix **R** are then recovered by RQ-decomposition. It is straightforward after this to recover the 'intrinsic parameters' pertaining to cameras properties, f/δ_x, f/δ_y, u_0 and v_0, and the 'extrinsic parameters' pertaining to the camera-object configuration, **R** and **t**. This process is called camera calibration.

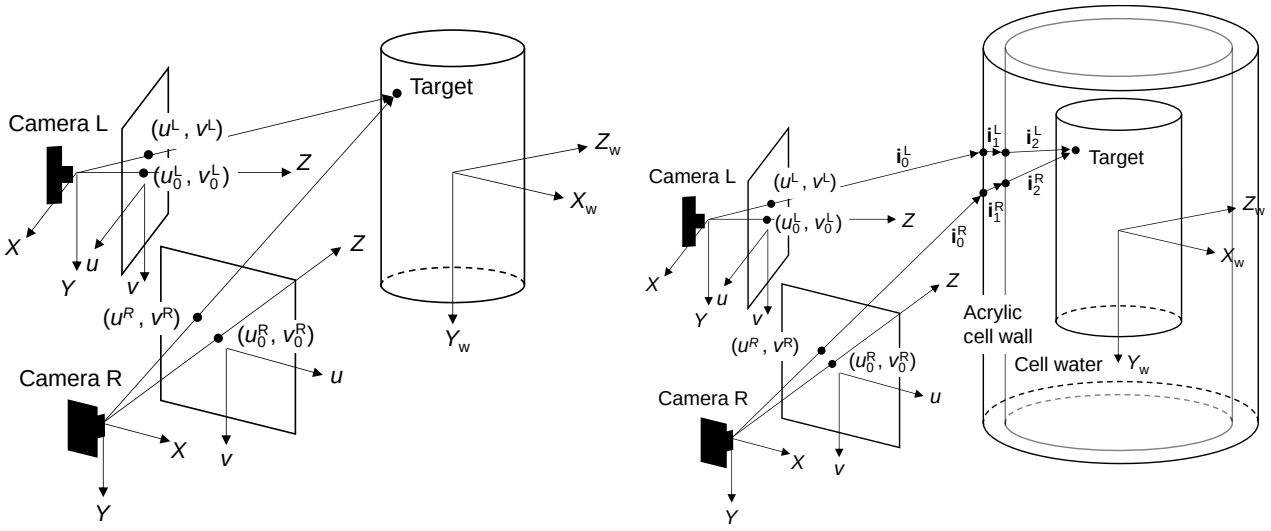

Figure 1: Geometry in stereophotogrammetry: (a) In air without optical ray refraction, (b) With cell wall and water causing optical ray refraction.

Stereo-matching and 3D reconstruction

Stereo-matching is a process of identifying a common point viewed by different cameras. In general stereophotogrammetry, pattern matching aided by epipolar constraints needs to be performed to find out the common point. To avoid this computation, this study proposes to adopt patterned target points, as shown in Figure 2. Due to the structured patterns (square grid in Figure 2, or staggered grid in Figure 3), it is straightforward to endow left-right common numbering to each target. A reference column and row are automatically identified by preparing targets with a different colour; see green and red columns in Figure 3. These targets are much easier to prepare than coded targets (e.g. Zhang et al., 2014), and can be populated more densely.

Once the coordinates (u^L, v^L) and (u^R, v^R) are obtained for a given target point in the left and right images, respectively, the pinhole camera model allows recovering (X_w, Y_w, Z_w) by the following equation:

$$\begin{bmatrix} p_{31}^L u^L - p_{11}^L & p_{32}^L u^L - p_{12}^L & p_{33}^L u^L - p_{13}^L \\ p_{31}^L v^L - p_{21}^L & p_{32}^L v^L - p_{22}^L & p_{33}^L v^L - p_{23}^L \\ p_{31}^R u^R - p_{11}^R & p_{32}^R u^R - p_{12}^R & p_{33}^R u^R - p_{13}^R \\ p_{31}^R v^R - p_{21}^R & p_{32}^R v^R - p_{22}^R & p_{33}^R v^R - p_{23}^R \end{bmatrix} \begin{bmatrix} X_w \\ Y_w \\ Z_w \end{bmatrix} = \begin{bmatrix} p_{14}^L - p_{34}^L u^L \\ p_{24}^L - p_{34}^L v^L \\ p_{14}^R - p_{34}^R u^R \\ p_{24}^R - p_{34}^R v^R \end{bmatrix} \quad (4)$$

This set of four equations for three unknowns is again an overdetermined system, and least-square optimisation is performed for deducing the best estimate of (X_w, Y_w, Z_w).

When there are interfaces, such as those between air and (acrylic) cell wall, and between cell wall and

water, along the ray travelling from the targets to the image sensor, correction for ray refraction needs to be added to the above pinhole camera model. The correction based on ray tracing was introduced by Bandhari et al. (2011) to triaxial testing, and incorporated to stereophotogrammetry by Zhang et al. (2014). The present study tried several different approaches, including correcting the 'refracted' images by direct mapping with polynomial functions. Among them, the ray tracing technique was found to be most accurate and easy to calibrate, and was therefore adopted. The vector tracing back the ray from the focal point, $\mathbf{i_0}$, in the X_w-Y_w-Z_w space is given as:

$$\mathbf{i}_0 = \begin{bmatrix} i_{0,X_w} \\ i_{0,Y_w} \\ i_{0,Z_w} \end{bmatrix} = -\mathbf{R}^{-1}\mathbf{t} + \eta \begin{bmatrix} \frac{\delta_u}{f}(u-u_0) \\ \frac{\delta_v}{f}(v-v_0) \\ 1 \end{bmatrix} \quad (\eta\text{: scalar}) \tag{5}$$

Tracing back the ray, this vector changes the direction twice, as it passes the two interfaces (to vectors $\mathbf{i_1}$ and $\mathbf{i_2}$ in Figure 1(b)). The direction after the refraction is given by Snell's law. Zhang et al.'s (2014) formulation of the 3D vector refraction facilitates this computation. The only input parameters for this computation are the absolute refraction indices for the air, n_a, acrylic cell wall, n_c, and water, n_w (1.00, 1.49 and 1.33, respectively), and outer and inner radii of the cell wall. The radii are used to compute the origin of $\mathbf{i_1}$ and $\mathbf{i_2}$. When the direction vector $\mathbf{i_2}$ =(i_{2,X_w}, i_{2,Y_w}, i_{2,Z_w}) and its origin (i.e. the exit point from the cell wall, (X_{w2}, Y_{w2}, Z_{w2})) are computed in this manner, the condition that this vector should go through the target (X_w, Y_w, Z_w) leads to the following:

$$\begin{bmatrix} i^L_{2,Y_w} & -i^L_{2,X_w} & 0 \\ 0 & i^L_{2,Z_w} & -i^L_{2,Y_w} \\ -i^L_{2,Z_w} & 0 & i^L_{2,X_w} \\ i^R_{2,Y_w} & -i^R_{2,X_w} & 0 \\ 0 & i^R_{2,Z_w} & -i^R_{2,Y_w} \\ -i^R_{2,Z_w} & 0 & i^R_{2,X_w} \end{bmatrix} \begin{bmatrix} X_w \\ Y_w \\ Z_w \end{bmatrix} = \begin{bmatrix} i^L_{2,Y_w}X^L_{w2} - i^L_{2,X_w}Y^L_{w2} \\ i^L_{2,Z_w}Y^L_{w2} - i^L_{2,Y_w}Z^L_{w2} \\ i^L_{2,X_w}Z^L_{w2} - i^L_{2,Z_w}X^L_{w2} \\ i^R_{2,Y_w}X^R_{w2} - i^R_{2,X_w}Y^R_{w2} \\ i^R_{2,Z_w}Y^R_{w2} - i^R_{2,Y_w}Z^R_{w2} \\ i^R_{2,X_w}Z^R_{w2} - i^R_{2,Z_w}X^R_{w2} \end{bmatrix} \tag{6}$$

The equation is again overdetermined, meaning that the rays from right and left cameras may not exactly meet at a point. Least-square optimisation provides the best estimate of (X_w, Y_w, Z_w). Either one of the first three rows, and either one of the last three rows in Eq.(6) are mathematically redundant. However, optimisation based on this set of six equations leads to much better accuracy in (X_w, Y_w, Z_w) reconstruction than with four. When Eq.(6) is applied to a case without refraction by setting n_a=n_c=n_w=1, almost same numerical results for (X_w, Y_w, Z_w) are obtained as by Eq.(4).

Zhang et al.'s (2014) approach is essentially to use more than two camera positions, which expands Eq.(6), thereby further increasing the accuracy in (X_w, Y_w, Z_w) reconstruction. Eq.(6), based only on two camera positions, sometimes led to notable inaccuracy in absolute positioning of the target, as discussed later. Zhang et al. (2014) quotes an accuracy of 0.056-0.076mm in their approach, while up to 1mm of offset was output by the current two-position approach. However, the accuracy of relative displacement measurement will be shown to be still very high in this approach. Having fixed camera positions, rather

than moving cameras to various positions, is advantageous in achieving high precision in continuous, relative displacement measurement. Even with constant re-calibration, dynamic camera positions inevitably generate artefact movements even in stationary objects.

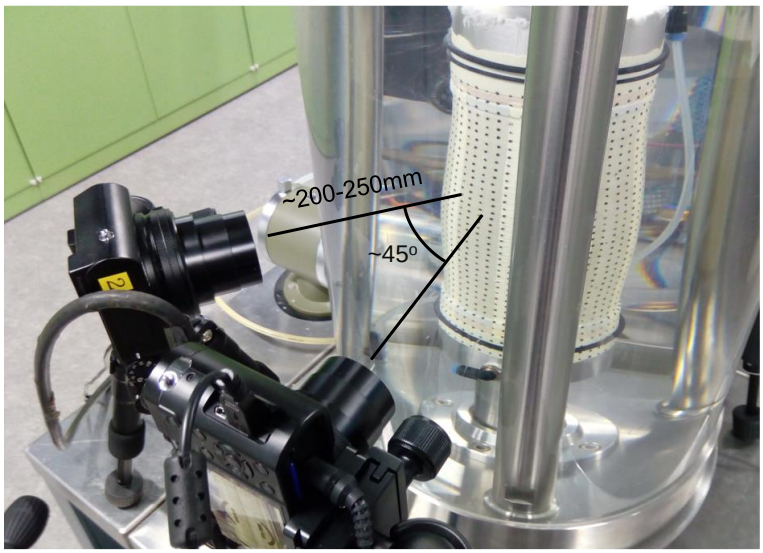

Figure 2: Square-grid pattern targets and typical camera alignment

TARGET TRACKING METHOD: ASSESSMENT OF PRECISION AND ACCURACY

Photographic conditions and validation exercise

The stereophotogrammetric theory, along with a target recognition routine to obtain (u, v) for Eq.(5) from images, was implemented into a computer code written in Python. The code uses OpenCV4.0 library for fast image processing. All the images in this study were taken with two pairs of identical digital cameras, Panasonic Lumix TX1, having a 1.0-inch, 20.1-Megapixel MOS image sensor and optical zoom. This is an affordable middle-grade compact-type model. Higher-grade cameras will improve the results modestly, but at much increased cost. The deployed cameras had a built-in time-lapse shooting function allowing continuous shooting without any auxiliary controller. All the photos were taken with 3,648pix by 4,864pix (meaning that 17.7 Magapixels were active). The images were saved as low-compression Jpeg. For all the conditions, including the validation exercise and the real soil testing discussed later, the following set of common photographic conditions was adopted. The images were taken with ISO 125, shutter speed of 1/5sec, focal length of 9mm and F-number of 8 under room lighting. The lens-object distance was around 200-250mm, and two cameras were horizontally aligned at around 45° angle to each other. As the movement of the object (soil or dummy) is usually very slow, a lower shutter speed is advantageous in alleviating the noise and hence improving the precision, due to the analogue low-pass filtering effect. The ISO value should be adjusted according to the room light intensity. Camera features such as automatic focus, mock shutter sound, image stabilizer, etc. were turned off to boost the image repeatability.

With these conditions, the accuracy and precision in 3D displacement measurement were firstly assessed by using a dummy cylinder. Here the accuracy is defined as closeness to the true displacement, while

the precision is defined by the scatter of results from multiple measurement attempts, following the definition, for example, by Germaine and Ladd (1988).

The accuracy was first assessed in the air (i.e. no refraction effect) by using a 3-degree-of-freedom (DOF) stage operated with 0.01mm-precision micrometers in each of X_w, Y_w and Z_w directions, as shown in Figure 3(a). A dummy stainless cylinder with 150mm in height and 75mm in diameter was placed and moved three-dimensionally by given amounts. A similar exercise was conducted next by submerging a PVC tube dummy into cell water. To avoid submerging the stage, the dummy-stage system was suspended from an overhead beam, as shown in Figure 3(b). As the 3-DOF stage was too large to suspend, a smaller 2-DOF (X_w-Z_w) stage was used instead for this case. The assessment in the Y_w-direction was therefore not conducted. The precision was assessed based on the scatter in displacement measurement of stationary targets.

Camera calibration was done with known initial coordinates of the target points themselves by using Eq.(3) when the view is refraction-free. When the cell is used, however, another set of targets is necessary outside the cell. A calibration sheet, with targets at known intervals, was attached to the outer surface of the cell in this case, as shown in Figure 3(c). In this manner, Eq.(3) can still be used for calibration.

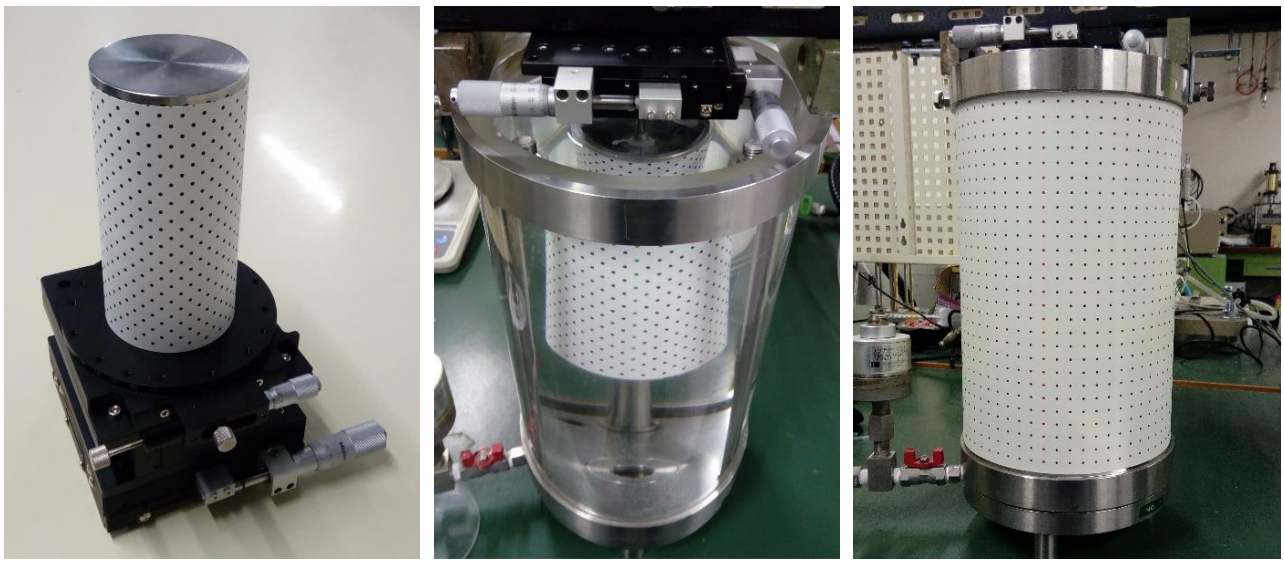

(a) (b) (c)

Figure 3: Displacement tracking tests by using dummy specimen and multi-DOF stages: (a) In air, with 3-DOF stage, (b) In cell water, with 2-DOF stage, (c) Calibration sheet outside the cell

Precision: Introduction of sub-pixel DIC in target tracking

Figure 4(a) shows examples of the images recorded with two cameras. The target points were extracted by binarising the images with adaptive Gaussian thresholding with appropriate threshold parameters, as shown in Figure 4(b). The block size of 4-6 times the target diameter and the threshold offset of 10-20

were used in this study. For each blob (i.e. a white pixel aggregate corresponding to a target), boundary pixels were detected and the centroid coordinates, size and the sphericity were computed in the *u*-*v* space. Unwanted noise pixels picked up by the binarisation was automatically discarded based on their size and sphericity anomaly. The centroid coordinates were recorded as the target coordinates, to be used as (u, v) in Eq.(5).

The precision of the 3D reconstruction largely depends on how precisely (u, v) can be read from images. As the blob size is dependent on the binarisation threshold and fluctuation in light intensity, some researchers (e.g. Qiao et al., 2008) prefer to work in greyscale, using a Gaussian particle template for objective and robust determination of target coordinates. In this study, however, the binarisation was found to have sub-pixel accuracy in determining the blob centroid, because each blob typically has as many pixels as a few thousands, and the centroid location is insensitive to modest boundary fluctuation. The thinner lines in Figure 5 shows examples of coordinates for five targets on a stationary dummy, observed continuously for 45 shots at 10-sec intervals. As movement of each particle is tracked, this is essentially Particle Tacking Velocimetry (PTV), with simple binarisation processing. Typically the scattering is within +/-0.3pixels.

The above precision is somewhat inferior to that achievable by sub-pixel Digital Image Correlation (DIC) (Nishimura et al., 2016). This study therefore proposes to adopt a hybrid approach, as illustrated in Figure 6. Firstly, images are binarised with arbitrary but appropriate threshold parameters, and the coordinates of each target are obtained, as explained above. This step provides a first estimate of the movement (Δu, Δv). Next, sub-pixel DIC is performed by using the greyscale target image from the previous step as interrogation window, and searching for the maximum correlation only at very close vicinity (+/-1 or +/-2 pixels) of the new coordinates estimated by (Δu, Δv). This method has same accuracy as standard sub-pixel DIC, but the searching effort is drastically reduced, because the binarisation and boundary-detection are relatively fast processes. This hybrid method is efficient without compromising the precision in eventual correlation optimisation at the sub-pixel level. It also helps avoid erroneous matching of targets even when they have indistinguishable geometric patterns, as there is only one candidate target within the limited searching range. The sub-pixel DIC adopted the same method as by Nishimura et al. (2016), using bi-quadratic approximation of the correlation coefficient surface in the *u*-*v* space. As a result, the precision is improved as shown with the thicker lines in Figure 5.

The precision is now evaluated in terms of reconstructed (X_w, Y_w, Z_w) by stereophogrammetry in Figure 7(a)-(c). In some cases, for example in Y_w in this case, monotonic drifts are observed, possibly due to camera warming and/or tripod creep. This is already seen in the camera image space, as in Figure 5(b). This effect is usually cancelled by considering relative displacement against one of the targets, as shown in Figure 7(d)-(f). The precision of the relative displacement, the key variable in strain calculation, was 0.002mm in ΔX_w and ΔY_w and 0.003mm in ΔZ_w when defined as the standard deviation from 45 recordings (images), and 0.001mm in ΔX_w and ΔY_w and 0.002mm in ΔZ_w when 5-point moving average was taken. Also shown in Figure 7(f) is the ΔZ_w values averaged over 4 adjacent points, indicating further

improved precision. When applied to triaxial testing, ΔZ_w is dominant on the radial displacement. Obviously, the strain can be resolved better over a wider domain represented with many target points, even when the precision for each individual target is limited.

Compared to a typical precision of 0.0001mm achieved by conventional local displacement transducers, such as Hall-effect sensors (Clayton and Katrush, 1986), LDTs (Goto et al., 1991) and LVDTs (Cuccovillo and Coop, 1997), the precision of the proposed system is still lower by one order. However, it has the clear advantage of being capable of following any large deformation as long as the object remains in sight. Soil testing is generally slow, and a sufficient number of continuous photographs are easily taken. The target movements are then very limited between images, and this removes a need for complex algorithm of particle (target) tracking usually required in hydrodynamics. In the actual tests discussed later, the rate of target mis-tracking was less than 0.01%, which is anyway easily detected and corrected automatically.

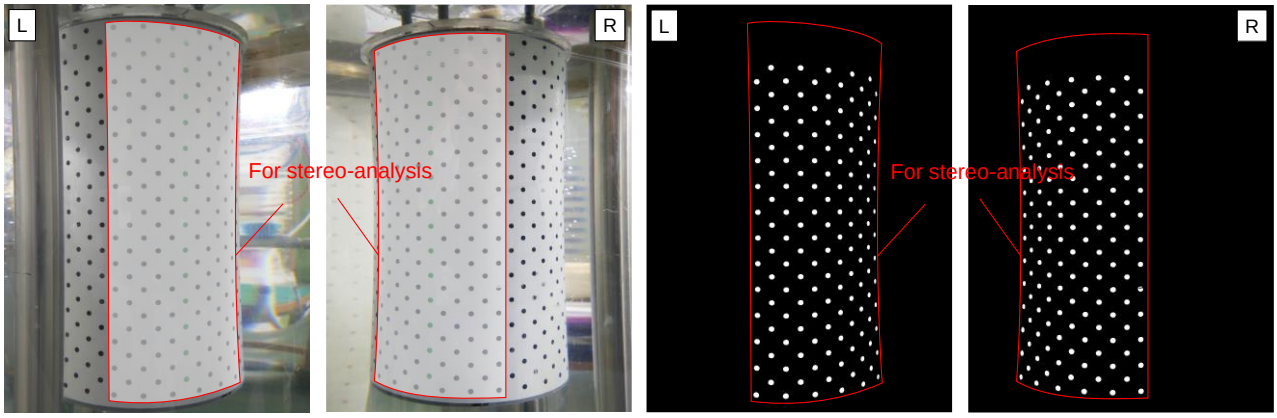

Figure 4: Examples of stereo-images: (a) Original images, (b) Binarised images.

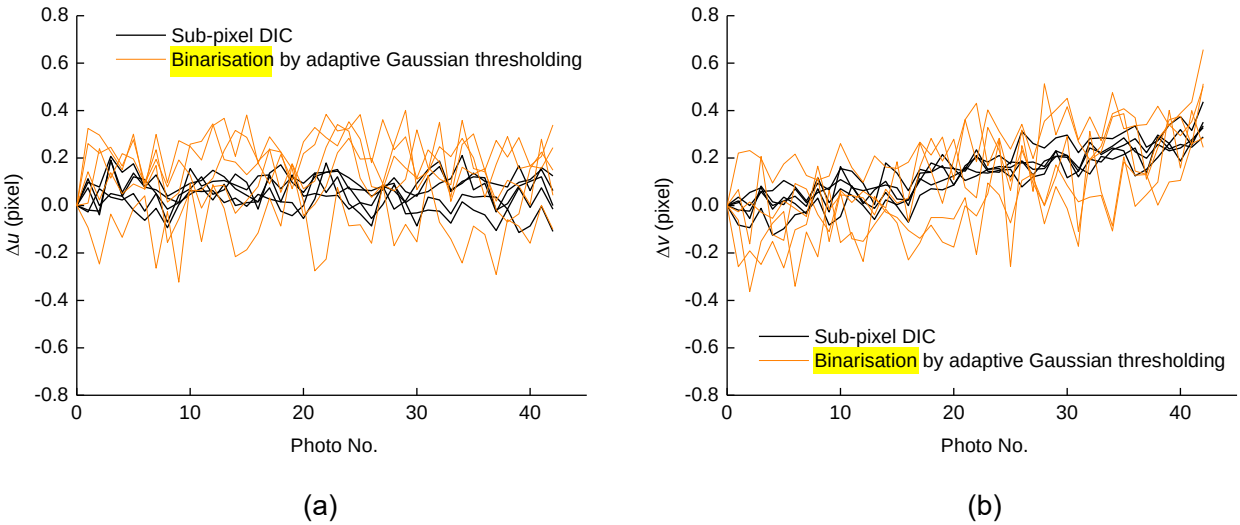

Figure 5: Examples of target coordinates extracted from images of stationary dummy: (a) Δ*u*, (b) Δ*v*.

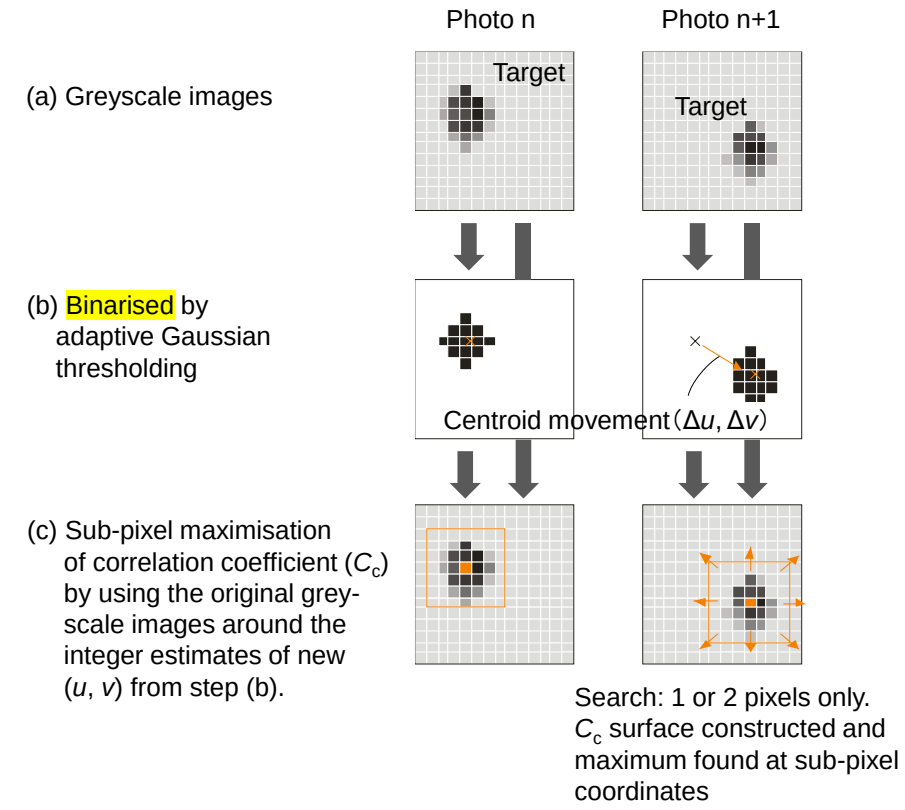

Figure 6: Hybrid approach to target recognition and tracking with sub-pixel precision

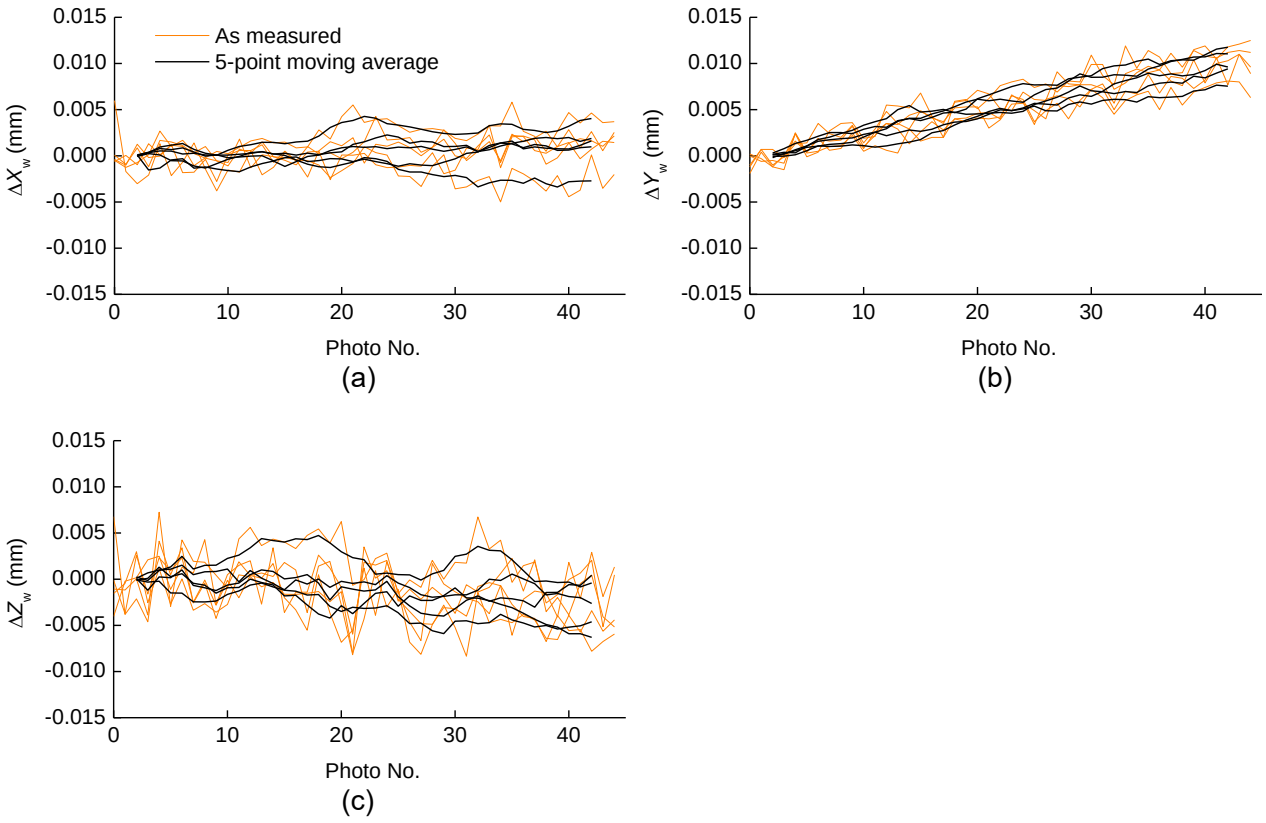

(*Figure continues to next page*)

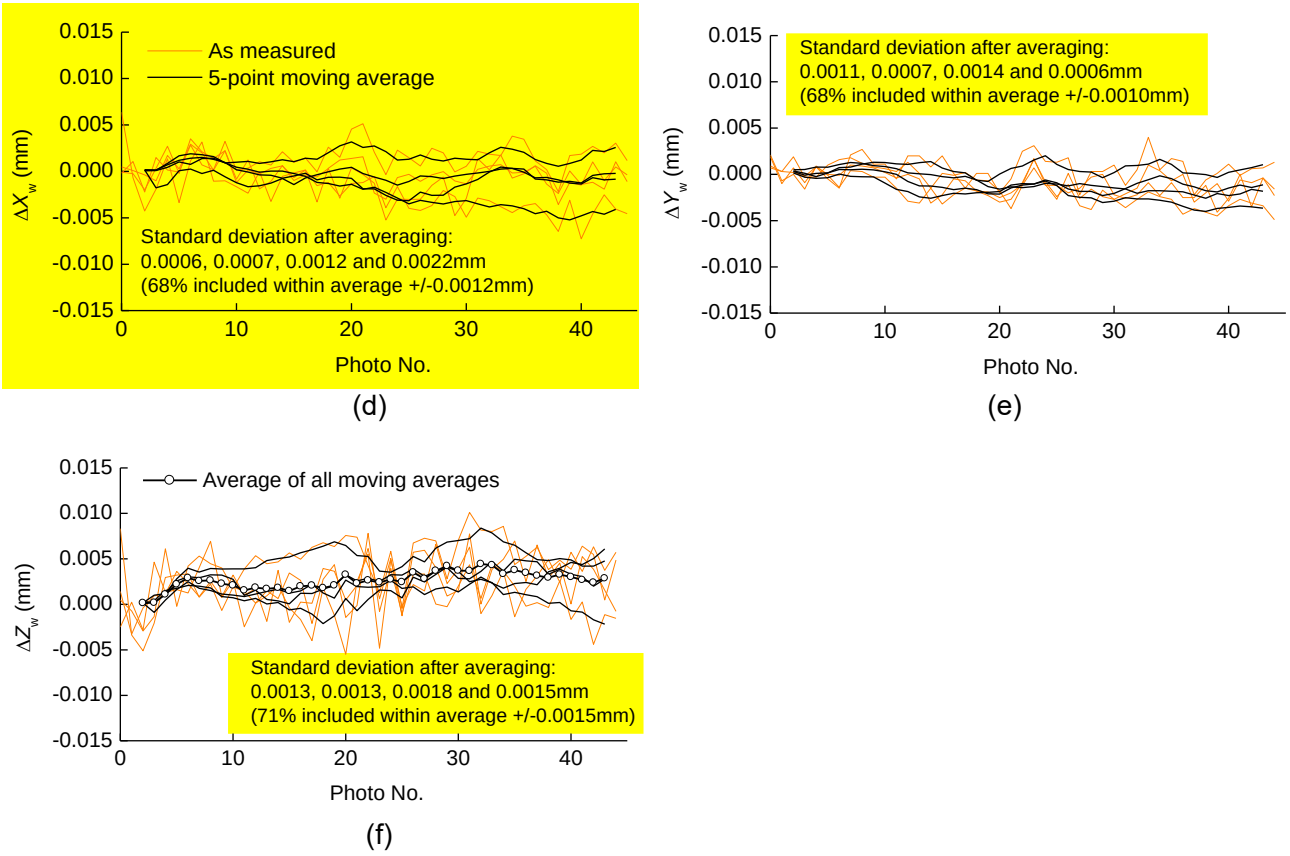

Figure 7: Examples of reconstructed displacements of stationary targets in X_w-Y_w-Z_w space: (a) Absolute displacement ΔX_w, (b) Absolute displacement ΔY_w, (c) Absolute displacement ΔZ_w, (d) Relative displacement ΔX_w, (e) Relative displacement ΔY_w, (f) Relative displacement ΔZ_w.

Accuracy

The stages were operated to give the dummy displacements of 0.05mm successively in X_w, Y_w and Z_w directions (no ΔY_w with the 2-DOF stage), and similar operations were repeated with 0.5mm and 5mm displacements. Figure 8 shows the intended path and the stereo-reconstruction for 2-DOF movements observed through cell water and cell wall. Their match, or the accuracy, is satisfactory at all the scales. Although the observed path appears to deviate immediately after (ΔX_w, ΔZ_w)=(0.05mm, 0.05mm), this is likely to be due to the manual operation of the stage, which gave the overhead beam an elastic deflection. The observed path returned to the ideal path once the hand was off the micrometer. The accuracy was quantitatively evaluated for 5mm displacements in each direction, as a larger displacement poses a more stringent test for the geometric (refraction) correction. The results are shown in Tables 1 and 2 for observation with and without refraction (i.e. with and without cell water/wall), respectively. For both cases, the accuracy is 1% of the 5-mm span, without any notable bias and cross-direction interference.

The above assessment was performed without cell pressure. Zhang et al. (2014) indicate that the cell wall can be deflected at elevated cell pressures, affecting the ray refraction. This aspect was investigated for the adopted cell by observing a rigid steel cylinder with the same dimensions as the soil specimen, while increasing the cell pressure from 0 to 400kPa. The outer diameter and the thickness of the acrylic

cell wall were 266mm and 18mm, respectively (the expected outer diameter increase is 0.1mm for 400kPa from elastic analysis; Timoshenko and Goodier, 1970). The apparent displacements, (X_w, Y_w, Z_w) attributable to the cell deflection were all less than 0.02mm, or 0.005mm/100kPa, across the viewed domain. These values are insignificant compared to the expected strains in soils for the same pressure variation, and hence no correction was made for this. The whole summary of the image analysis processes is given in Figure 9.

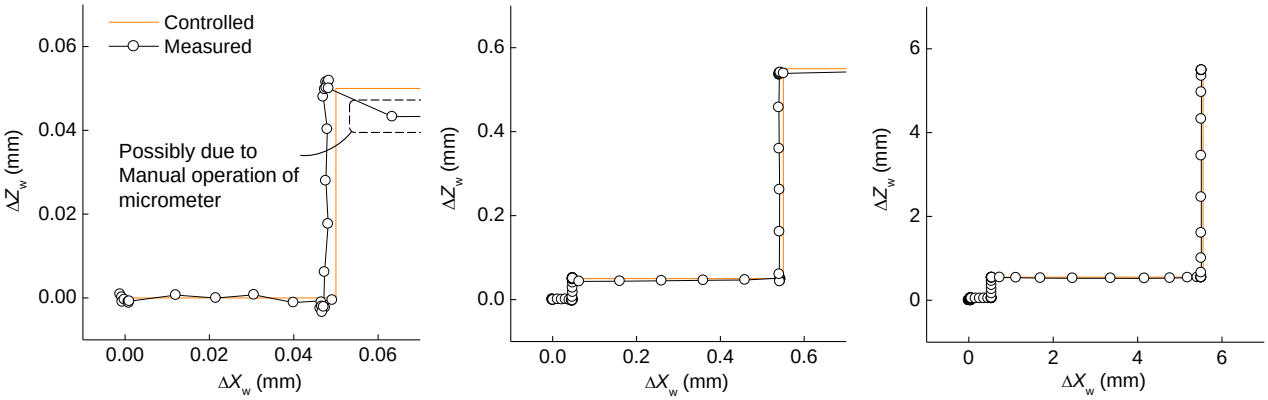

Figure 8: Comparison of controlled and reconstructed X_w-Z_w paths of targets on water-submerged dummy: Shown at three scales. Note that the controlled path accuracy is not guaranteed below 0.01mm.

Table 1: Observed displacement against 5mm displacement given in each direction: Average and standard deviation (in the backets) for 154 target points in sight. Targets in air.

		Given displacement		
		ΔX_w	ΔY_w	ΔZ_w
Measured displacement	ΔX_w	+100.8% (0.4%)	-0.3% (0.0%)	+0.2% (0.1%)
	ΔY_w	-0.1% (0.2%)	+100.1% (0.2%)	-0.3% (0.1%)
	ΔZ_w	-0.0% (0.2%)	+0.1% (+0.2%)	+100.1% (0.3%)

Table 2: Observed displacement against 5mm displacement given in each direction: Average and standard deviation (in the backets) for 143 target points in sight. Targets in cell water.

		Given displacement	
		ΔX_w	ΔZ_w
Measured displacement	ΔX_w	+100.1% (0.3%)	+0.1% (0.2%)
	ΔY_w	+0.4% (0.2%)	-0.1% (0.3%)
	ΔZ_w	-0.1% (0.5%)	+98.9% (0.4%)

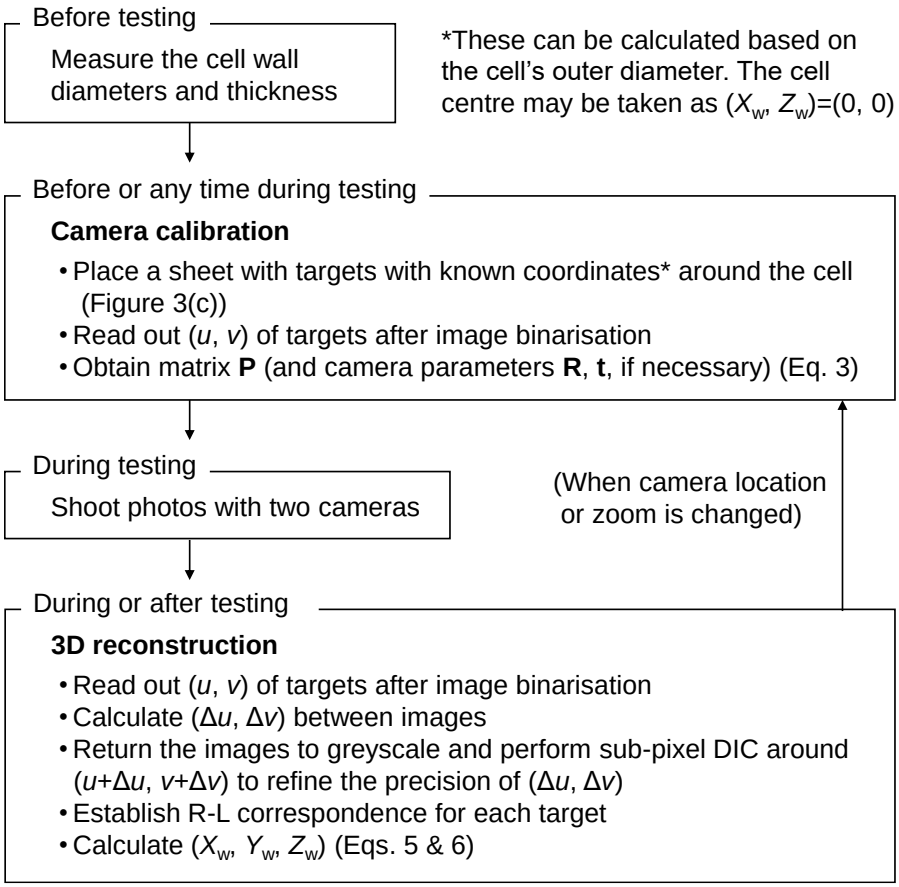

Figure 9: Summary of proposed 3D coordinates measurement processes

APPLICATION TO TRIAXIAL TESTING: DEFORMATION OF CLAY SAMPLES

Material, testing method and strain calculation

The described displacement measurement system was applied to triaxial testing on clay samples for demonstration. The tested samples were reconstituted Kasaoka clay. The clay had plastic and liquid limits of 26% and 60%, respectively, and the fractions below 2μm and 63μm were 40% and 100%, respectively. It was pre-consolidated one-dimensionally from slurry to the vertical effective tress σ_{vc}'=200kPa in a consolidometer, trimmed to 150mm in height (H) and 75mm in diameter and transferred to triaxial apparatus after eight strips of filter paper were attached to the lateral surface for drainage. Figure 10 shows the initial target coordinates for one of the tests, as reconstructed by stereophotogrammetry. Each camera pair had a stereo-view over 1/4 of the whole specimen perimeter. Each view is called Front, Rear, Right and Left faces below. Some views were overlapping, while there was a part not observed at all, where the drainage tube from the top cap covered the surface. There was discrepancy of up to 1mm where targets overlap, as discussed earlier.

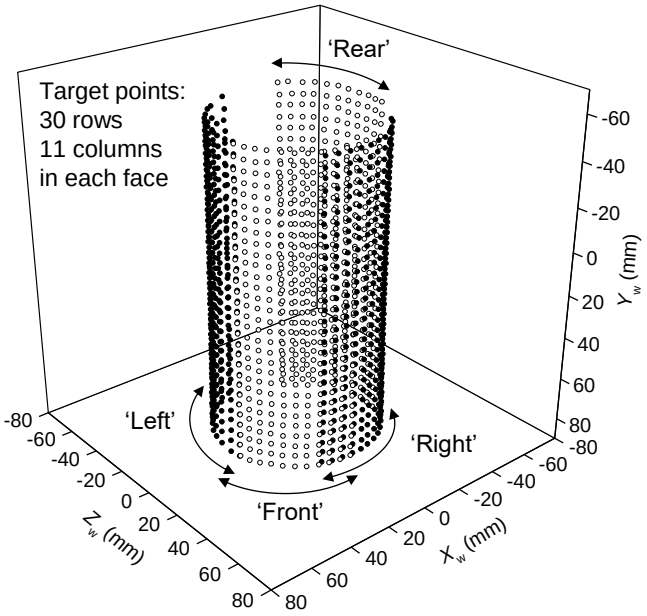

Figure 10: 3D coordinates of target points reconstructed from four-face observation (example of Test NL)

The sample was first set at the mean effective stress p'=70kPa (≈$\sigma_{vc}'/3$, which was known by experience for this clay to cause negligible initial strain). The sample was then subjected to (i) three cycles of undrained small-strain axial loading to axial strain ε_a=0.05% and then unloading to the origin at strain rate $\dot{\varepsilon}_a$=0.2%/hour, (ii) isotropic compression to p'=300kPa at 8kPa/hour, (iii) some 2,700-min. creep, (iv) isotropic swelling to p'=250kPa at -8kPa/hour, (v) same three cycles as (i), and then (vi) undrained axial loading to ε_a=15% at $\dot{\varepsilon}_a$=0.6%/hour. In (i) and (v), the first cycle was a dummy cycle to give the second and third cycles a same recent stress history. The Front and Rear faces were observed in the second cycle, and the Right and Left faces in the third. Note that the above values for ε_a were externally controlled values, and the true internal strains were smaller than this. Given this, the ε_a=0.05% cycles were mostly within the 'Y2' surface defined by Jardine (1992), and sufficiently small to give the second and third cycles identical behaviour. The creep and the modest swelling in (iii) and (iv) cancelled the background creep rate to a level negligible to the subsequent loading (Nishimura, 2014a), with volumetric strain rate smaller than 0.001%/hour. During stages (ii)-(iv) and (vi), only the Front and Rear faces were observed with two pairs of cameras.

The adopted triaxial apparatus is described by Nishimura (2014a), but with all the local instrumentation removed for better sights of the specimen's lateral surface. The axial ram was driven by a direct-drive motor controlled at resolution of 150nm axial displacement. The top and bottom loading platens had a polished stainless steel surface. Here two tests were conducted: Case NL (Non-Lubricated), in which the clay specimen was directly placed on the platen, and Case L (Lubricated), in which the two ends were lubricated with a 0.1mm-thick Teflon sheet and a 0.3mm-thick latex membrane sheet (with the Teflon on the platen-side), put together with silicone grease. This arrangement reduces the interface friction

coefficient to 0.005 (friction angle of 0.3°) over the normal stress range 0-1500kPa.

The strains are all defined positive in compression, and calculated with the initial state at each of stage (i)-(vi) as reference. In deducing axial, radial and circumferential strains, ε_a, ε_r and ε_θ, from the observed target displacements, the calculation shown in Figure 11 was adopted and shown for each element defined by four target points. Note that ε_r defined in this manner is nominal, as it is affected by rigid-body movement. For small-strain loading stages, ε_a was deduced instead by regression to the vertical displacement profiles (ΔY_w-Y_w relationship) either over the whole specimen height H or its middle third $H/3$. The strains were also calculated based on the globally (externally) measured axial ram displacement and the global specimen volume change measured by a double-tube burette. Thus obtained ε_a and the volumetric strain ε_v were used to calculate the global radial strain ε_r by:

$$\varepsilon_r = \sqrt{\frac{1-\varepsilon_v}{1-\varepsilon_a}} \tag{7}$$

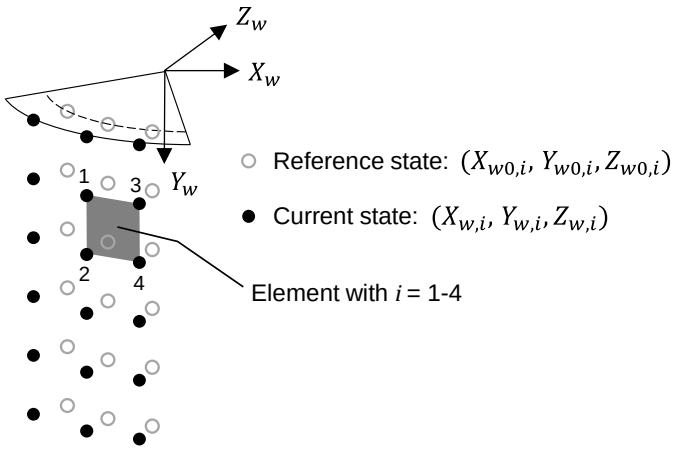

$$\varepsilon_a = -\frac{1}{2}\sum_{i=1}^{2}\frac{(Y_{w,2i}-Y_{w,2i-1})-(Y_{w0,2i}-Y_{w0,2i-1})}{Y_{w0,2i}-Y_{w0,2i-1}} \qquad \varepsilon_r = -\frac{1}{4}\sum_{i=1}^{4}\frac{\sqrt{X_{w,i}^2+Z_{w,i}^2}-\sqrt{X_{w0,i}^2+Z_{w0,i}^2}}{\sqrt{X_{w0,i}^2+Z_{w0,i}^2}}$$

$$\varepsilon_\theta = -\frac{1}{2}\sum_{i=1}^{2}\frac{\sqrt{(X_{w,i}-X_{w,i+2})^2+(Z_{w,i}-Z_{w,i+2})^2}-\sqrt{(X_{w0,i}-X_{w0,i+2})^2+(Z_{w0,i}-Z_{w0,i+2})^2}}{\sqrt{(X_{w0,i}-X_{w0,i+2})^2+(Z_{w0,i}-Z_{w0,i+2})^2}}$$

Figure 11: Calculation of normal strains at specimen surface from reconstructed X_w-Y_w-Z_w coordinates

Consolidation, creep and swelling stages

The strains observed during the consolidation, creep and swelling stages are shown in Figure 12 on the surface geometry observed at the end. They are also shown as profile in Figure 13, by taking row-wise averages. The horizontal strains (ε_r and ε_θ) were greater than ε_a due to anisotropy both in Case NL and

L. The influence of the end friction is clear in Case NL, in which the specimen ends underwent notably smaller ε_r and ε_θ. Interestingly, ε_a is greatest at around 10-20mm from the ends. This may be due to the friction-caused shear strain γ_{ar} contributing to negative dilatancy during normal compression to p'=300kPa. The bands at 10-20mm away from the ends may be where this effect minus the end-constraint effect decaying with distance sets a maximum. Cui et al. (2020) also observed concentration of axial stress at some distance from the ends in numerical analysis. Another interesting feature is that the effect of filter paper strips appears only on ε_θ. This gives an overall impression that ε_θ is highly non-uniform. Zhao et al. (2020) noted that the soil and membrane are in good coupling except at extremely low confining stress (as under liquefaction). The present study adds to this exception localities around the filter paper strips, where the membrane may not reflect the soil's local strain. However, the average over the specimen surface still provides meaningful values, as discussed below.

The entire Front and Rear face averages of strains are shown in Figure 14 against p'. The strains from the image analysis are fairly consistent with those from the global measurements. However, the image-based values for ε_r and ε_θ were not completely identical. One explanation for this is that the specimen behaviour was not perfectly axi-symmetric and the two-face (i.e. Front and Rear) observation failed to capture the entire strain to full. Indeed, the discrepancy is greater in Case L, where the specimen's central axis translated slightly during the test owing to the end lubrication. In this apparatus, the specimens always tended to move slightly to the direction of Front-Right face, perhaps due to innate imperfection in the apparatus alignment. The circumferential strain ε_θ is by definition unaffected by rigid-body movement, and also more precisely measured, as the displacements parallel to the image plane are dominant. Where ε_r and ε_θ are not consistent from images, the latter may be a better representation of the horizontal strain.

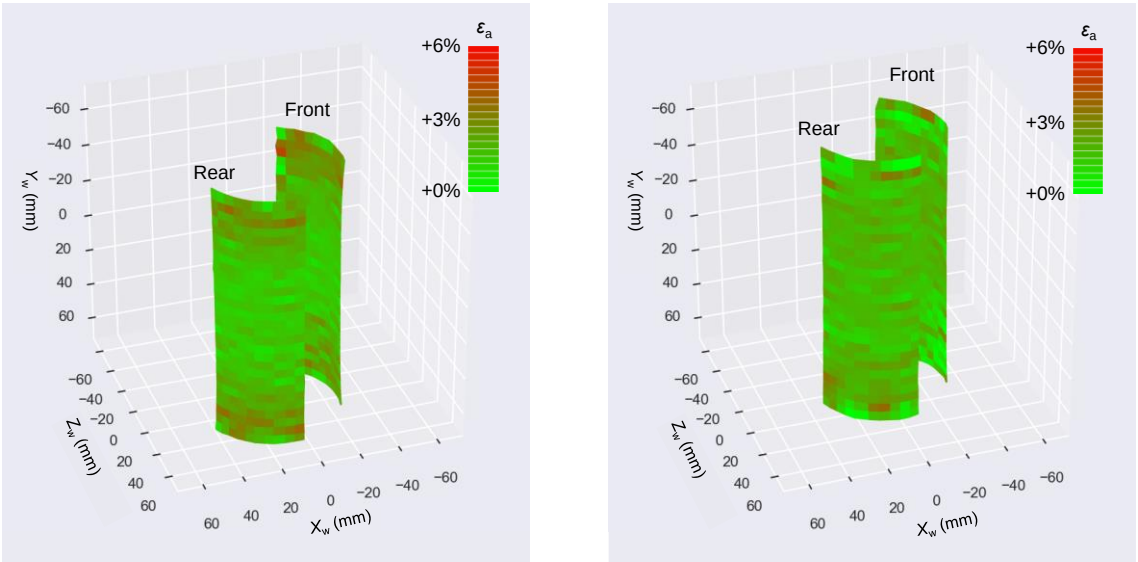

(a)

(*Figure continues to next page*)

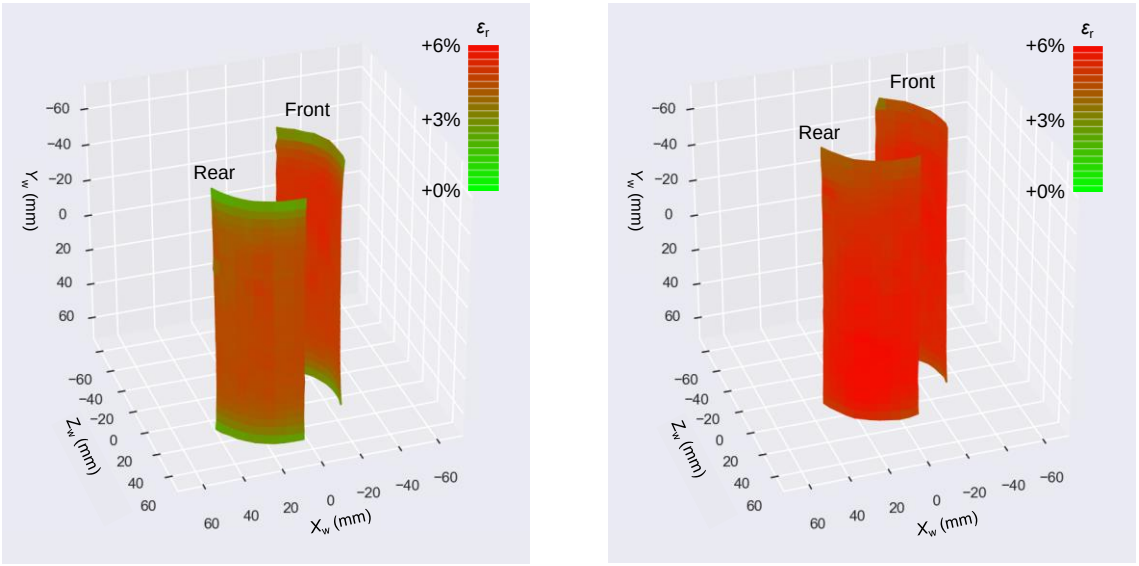

(b)

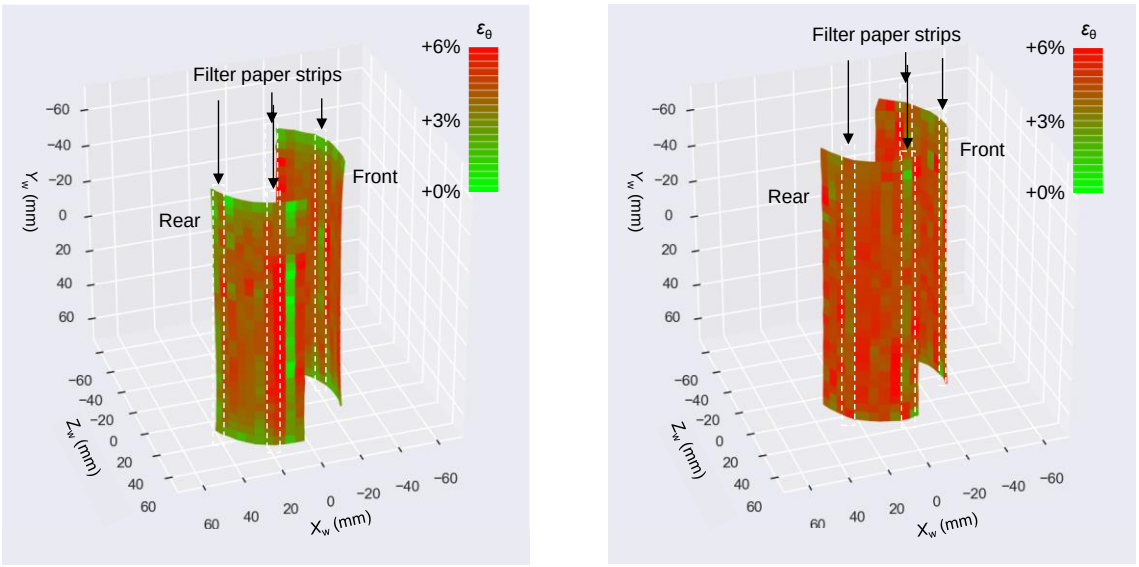

(c)

Figure 12: Strain distributions due to consolidation and swelling: (a) Axial strain, ε_a, (b) Radial strain, ε_r, (c) Circumferential strain, ε_θ (Left: Non-lubricated Case NL, Right: Lubricated Case L).

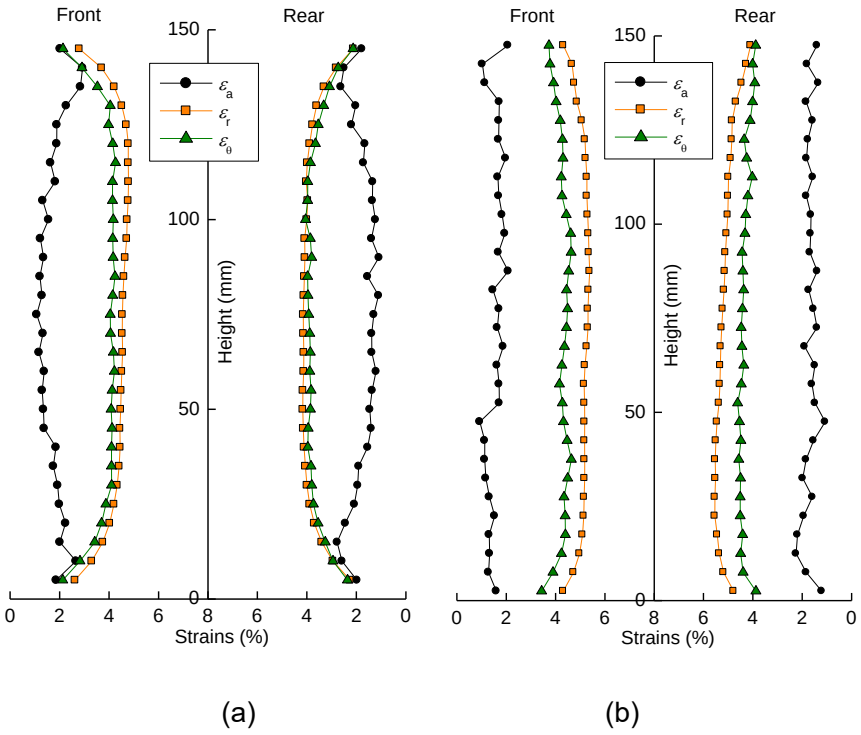

Figure 13: Profiles of strains due to consolidation and swelling (plotted against initial height): (a) Non-lubricated Case NL, (b) Lubricated Case L.

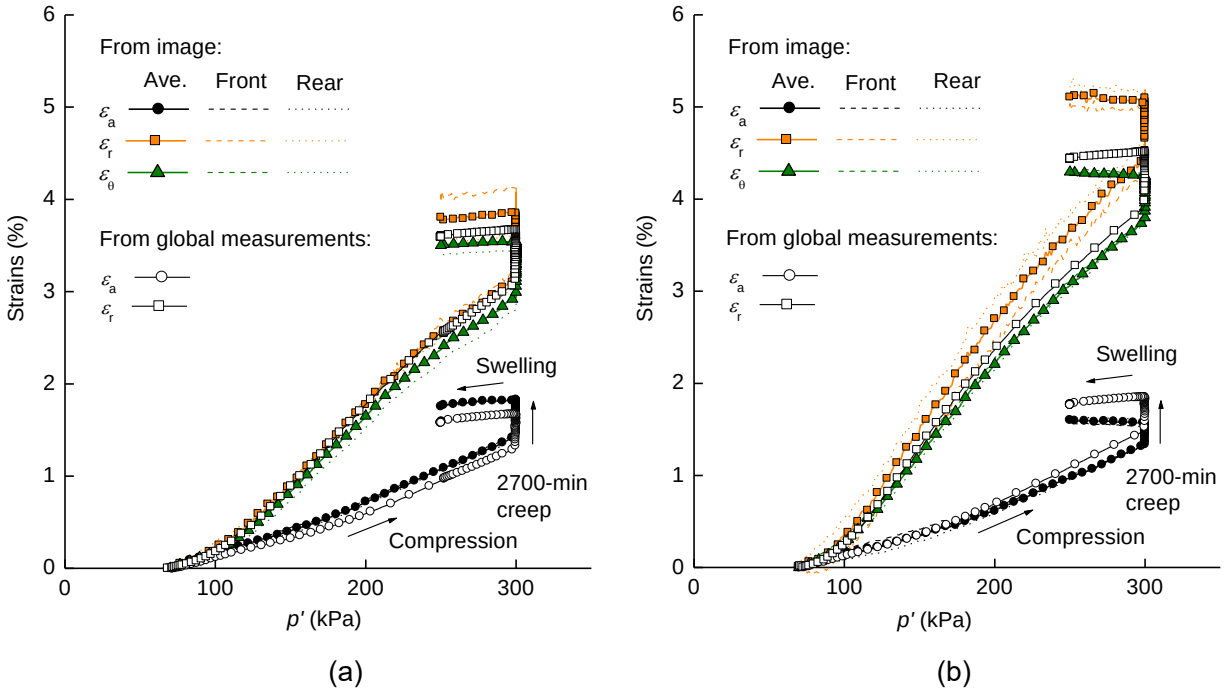

Figure 14: Comparison of strains during consolidation and swelling between image-based and global measurement-based computation: (a) Non-lubricated Case NL, (b) Lubricated Case L.

Small-strain axial loading/unloading cycle stages

Each cycle was analysed with 360 photographs, taken at 5-sec intervals. Examples of the observed deviator stress, q - axial stain ε_a curves, taken from p'=250kPa in Case NL, are shown in Figure 15. The middle $H/3$ of the specimen was used for ε_a calculation in this figure. Although ε_a based on the ram movement (global measurement) had extremely high precision, it was not accurate, being subject to the bedding error and apparatus compliances. The image analysis bypassed these error sources, and output much stiffer responses typically seen with local displacement transducers. The profiles of vertical displacement ΔY_w at selected moments during small-strain loading from p'=250kPa are shown in Figure 16. Although it may not be immediately clear from these profiles, regression to the whole specimen height H and the middle third leads to slightly greater strains in the latter, and hence smaller stiffness. Table 3 shows secant undrained Young's modulus $E_{u,sec}$ at ε_a=0.01%, calculated over H and $H/3$. The difference is smaller when the end lubrication is applied. It is also clear that measuring over the middle third does not compensate the end friction effect, at least in undrained conditions. The $E_{u,sec}$ values are still some 30% higher in the non-lubricated case NL. This magnitude of stiffness over-estimation due to the end friction has also been noted by Liu (2018) and Vinck et al. (2019) for sand. It is recommended that the mid-part measurement *and* end lubrication be both adopted. This conclusion is different from that on the strength, which is determined by more localised mechanisms. Bishop and Green (1965) noted that the shear strength is unaffected by the end condition when height-to-diameter is greater than 2.

The strain path for the same example is shown in form of ε_a against $(\varepsilon_r+\varepsilon_\theta)/2$ in Figure 17, calculated over whole H. The reference line indicates the slope -0.5, representing undrained (constant-volume) conditions. The results measured from images are broadly consistent with the reference line. Nishimura (2014b) observed that drained Poisson's ratio remains constant up to axial strain of 0.05% in clays. The image-analysis is therefore likely to capture true Poisson's ratio associated with smaller strains. The ε_a vs. $-(\varepsilon_r+\varepsilon_\theta)/2$ slopes, or undrained Poisson's ratio ν_u, were calculated for both Cases NL and L, either by observing the whole specimen height H or the middle third, as summarised in Table 4. Ideally, the undrained conditions mean ν_u=0.5 when the whole height H is analysed. Compared to this, the results were not conclusive. Overall, the middle third seems to give greater ν_u (lateral bulging), and its effect is more pronounced in Case NL, but with exception at p'=250kPa, Case L. As Nishimura (2014b) attempted, performing more cycles and taking average might have improved the confidence.

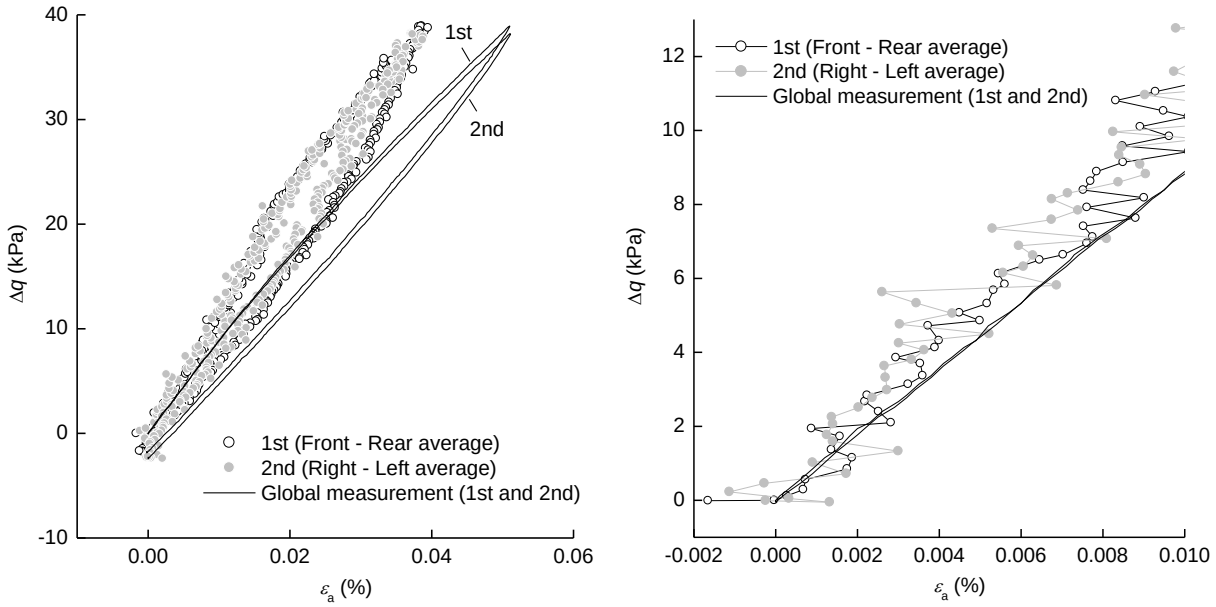

Figure 15: Deviator stress – axial strain relationships during small-strain loading-unloading (at p'=250kPa, lubricated Case L): (a) Full range, (b) Magnified. Images over $H/3$ were analysed.

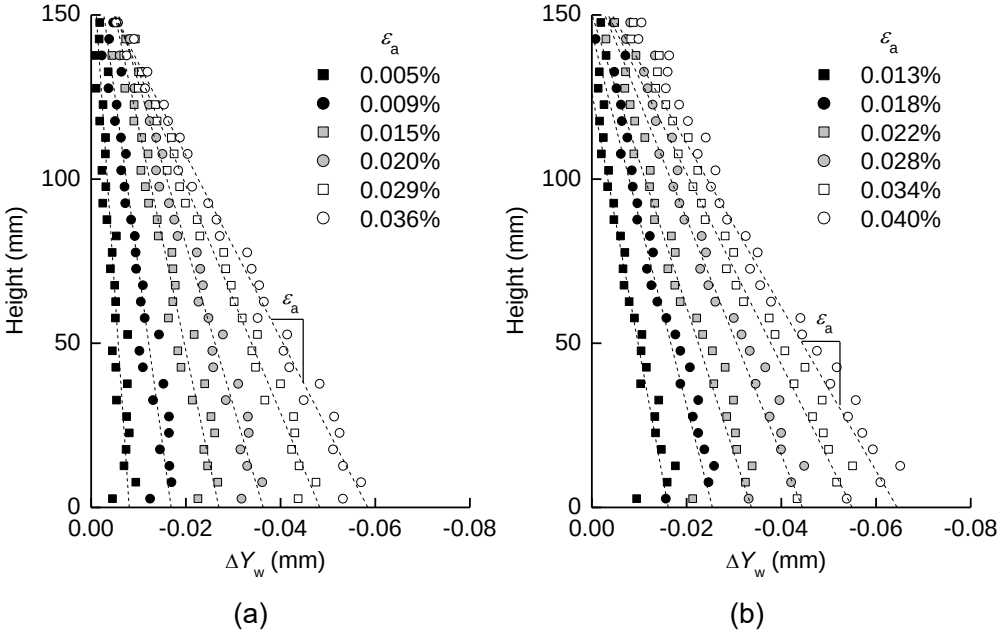

Figure 16: Profiles of vertical displacement ΔY_w during small-strain loading-unloading at p'=250kPa: (a) Non-lubricated Case NL, (b) Lubricated Case L.

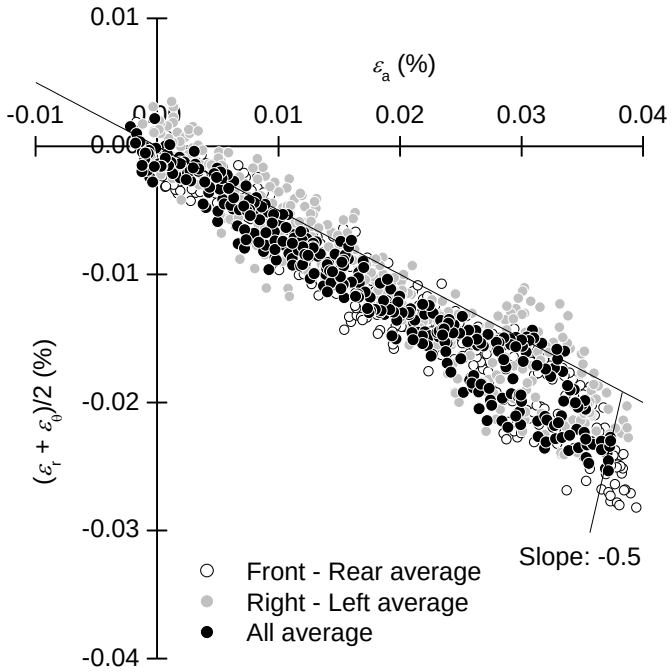

Figure 17: Strain paths during small-strain loading-unloading (at p'=250kPa, with end lubrication), computed for whole specimen height H

Table 3: Secant undrained Young's modulus $E_{u,sec}$ at ε_a = 0.01% from image analysis (Unit: MPa)

Domain for calculation	Without lubrication (Case NL)		With lubrication (Case N)	
	p' =70kPa	p' =250kPa	p' =70kPa	p' =250kPa
Over H	52	154	38	120
Over middle H/3	46	134	36	108
(Global measurement)	38	125	33	88
(Void ratio)	1.038	0.914	1.114	0.923

Table 4: Poisson's ratios from image analysis for undrained axial loading-unloading (ε_a to 0.05%)

Domain for calculation	Without lubrication (Case NL)		With lubrication (Case N)	
	p' =70kPa	p' =250kPa	p' =70kPa	p' =250kPa
Over H	0.418	0.570	0.595	0.588
Over middle H/3	0.536	0.657	0.634	0.533

Monotonic axial loading to large strain

The strains observed during the undrained loading to ε_a=15% are shown in Figure 18 on the surface geometry observed at the end. The photographs were taken every 30 seconds for ε_a<1% (200 photographs) and every 10 minutes for 1%<ε_a<15% (140 photographs). Their row-wise averages are shown as profile in Figure 19. The effect of end lubrication is clear, allowing the strains to distribute more uniformly across the specimen. Again, only ε_θ measurement is locally affected by filter paper strips. The comparison between the overall average strains from images and global measurements is shown in Figure 20. While good consistency between them was observed in Case NL, there was a notable discrepancy in ε_r in Case L. The nominal radial strain (=radial displacement/initial radius; see Figure 11) is clearly greater in the Rear face, suggesting a significant rigid-body translation due to end lubrication. In theory, this effect can be cancelled out by taking average of the data on the Front and Rear faces. In practice, however, some degree of error inevitably remains. Even under such conditions, ε_θ is insensitive to the horizontal translation and provides values consistent with the global measurement when integrated over the entire specimen.

Figure 21 shows the stiffness degradation curves, or $E_{u,sec} - \varepsilon_a$ curves synthesised from the small-strain loading data and the monotonic loading data, both deduced from images. The trends for $E_{u,sec}$ are resolvable down to around 0.005%. The chart by Vucetic and Dobry (1991) indicates that the secant stiffness at a strain of 0.01% is around 90% of the maximum value for clay with a plasticity index of 30, or for many other soils (Vardanega and Bolton, 2013). The curves obtained from the images fit this trend. If the photo-shooting interval is reduced, the monotonic loading alone could well have been capable of outputting the curve from 0.005% with sufficient confidence.

Currently the proposed stereophotogrammetric method with general consumer cameras is not capable of observing stiffness at strains further smaller than shown in Figure 21, at least under realistic testing conditions. The quoted strain level, 0.005%, is beyond the ‘elastic threshold’ for many soils. In this point, the method does not replace more precise local sensors, such as LVDTs, which are capable of resolving the behaviour to strains smaller by one more order. However, it is probably fair to claim that the curves in Figure 21 are helpful, or even sufficient, in deriving appropriate design curves. The proposed method can thus be a practical option in commercial laboratories, not just a novelty in research laboratories.

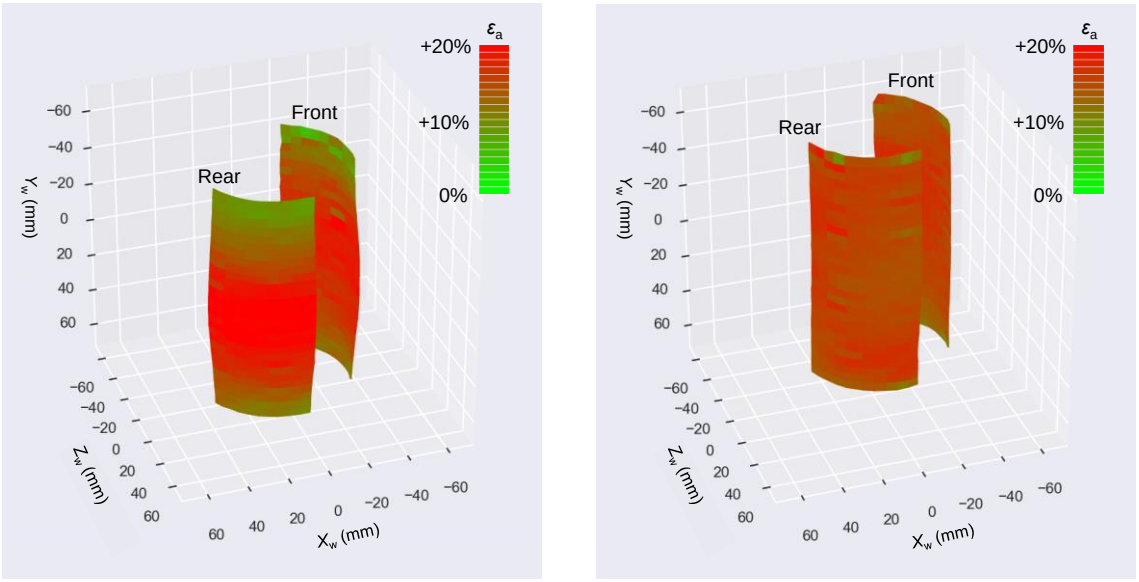

(a)

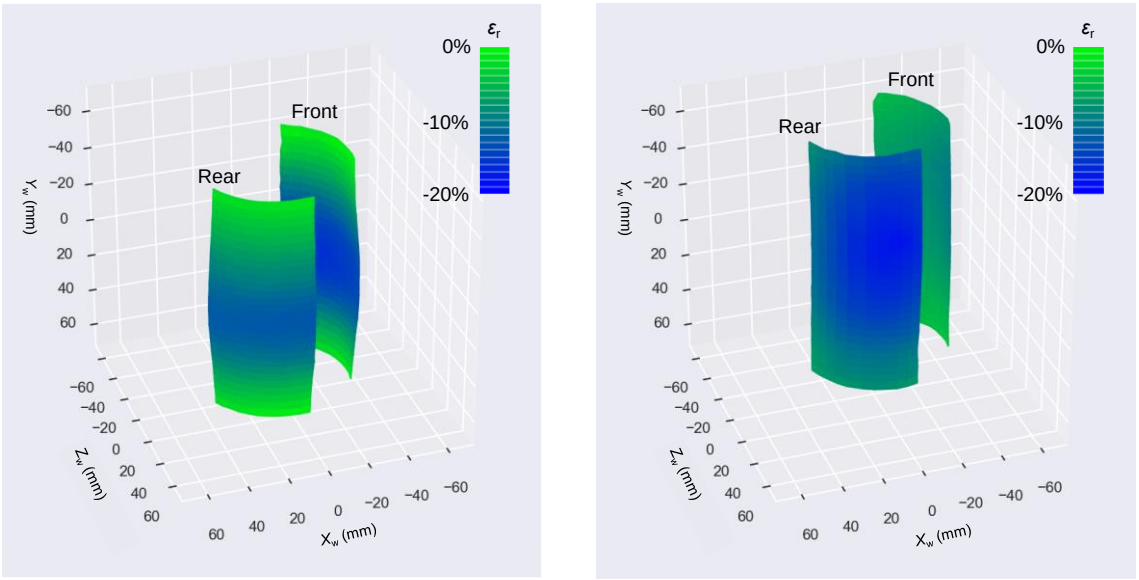

(b)

(*Figure continues to next page*)

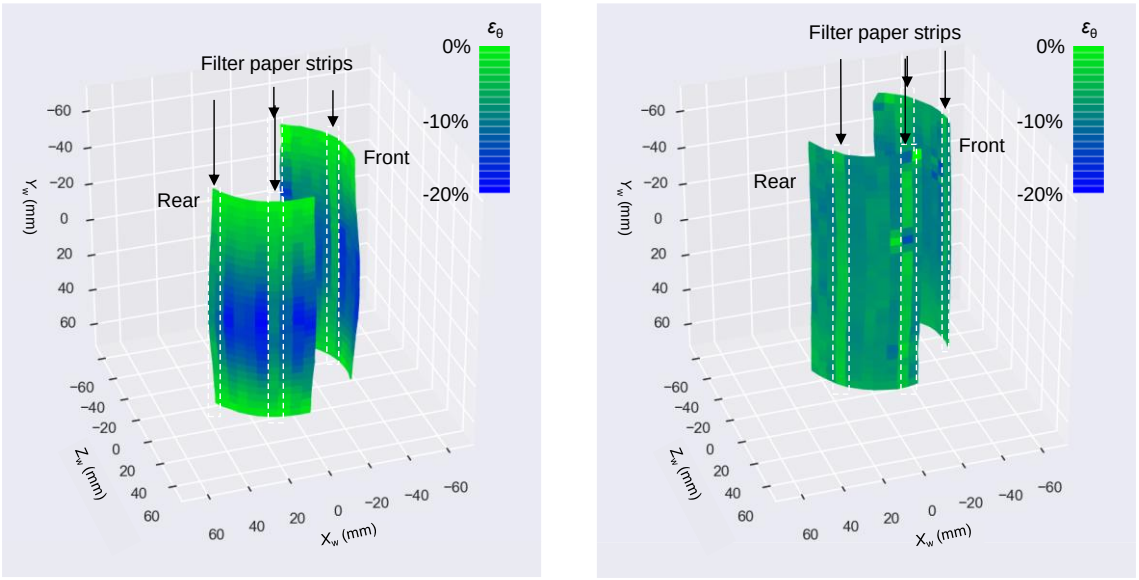

(c)

Figure 18: Strain distributions due to undrained triaxial compression: (a) Axial strain, ε_a, (b) Radial strain, ε_r, (c) Circumferential strain, ε_θ (Left: Non-lubricated Case NL, Right: Lubricated Case L).

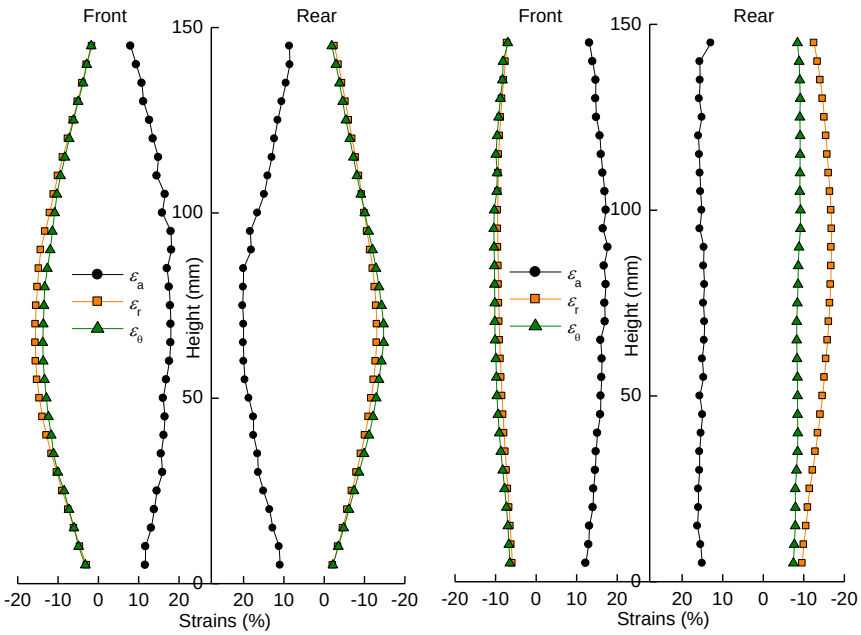

Figure 19: Profiles of strains due to undrained triaxial compression (plotted against initial height): (a) Non-lubricated Case NL, (b) Lubricated Case L.

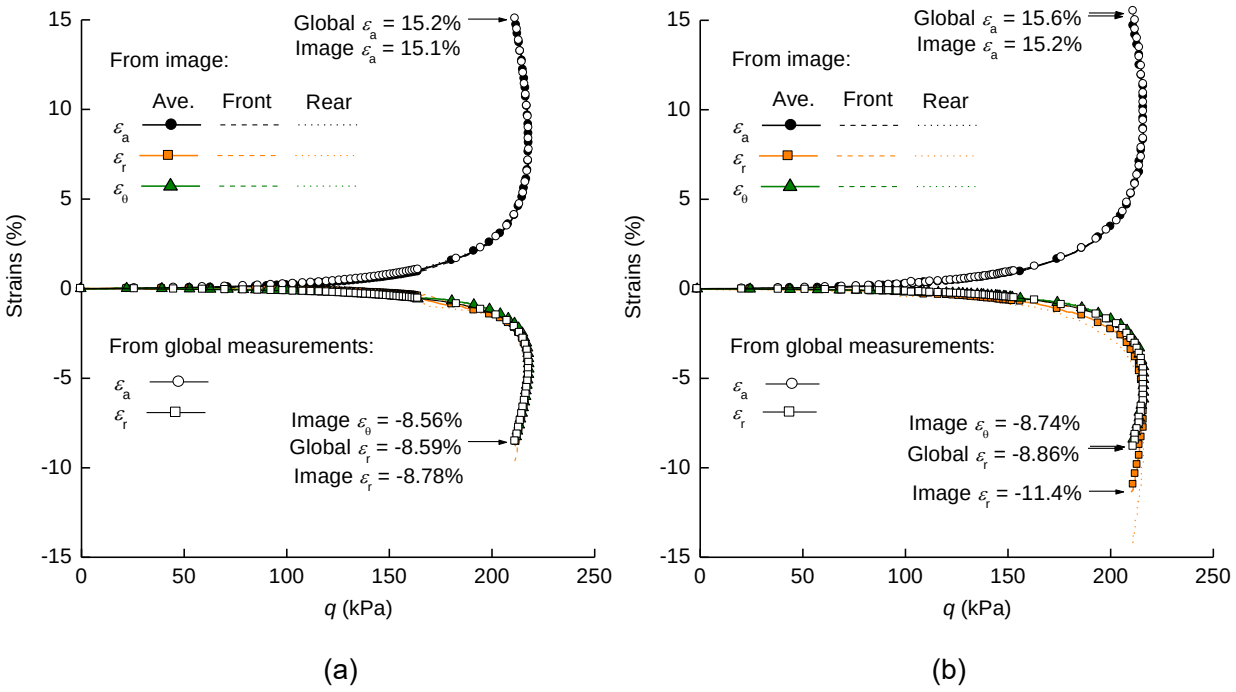

Figure 20: Comparison of strains during undrained triaxial compression between image-based and global measurement-based computation: (a) Non-lubricated Case NL, (b) Lubricated Case L.

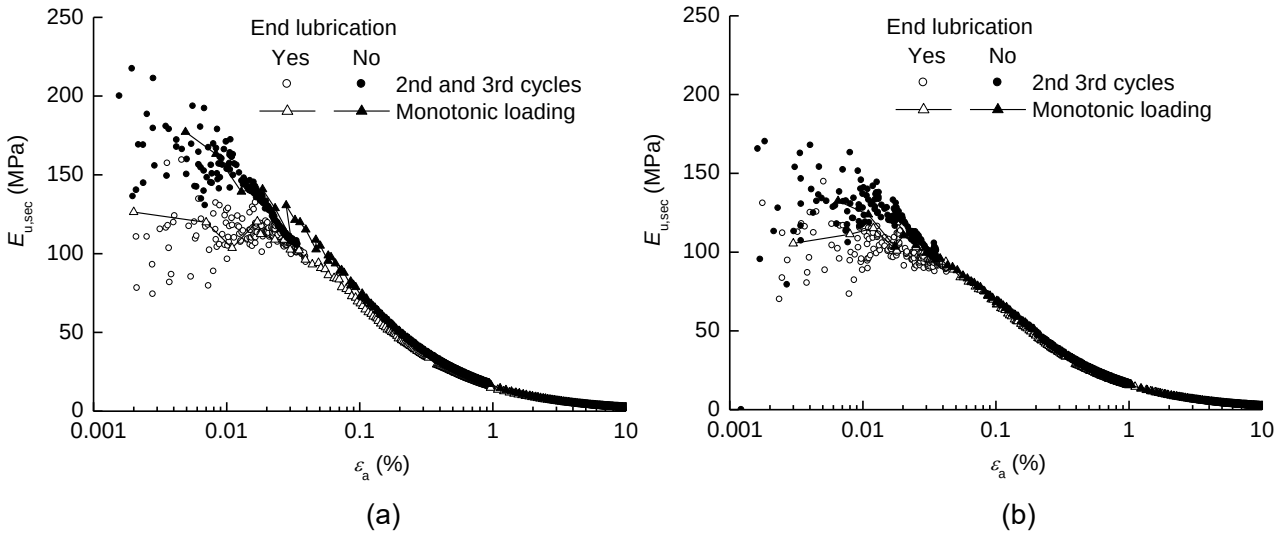

Figure 21: Secant undrained Young's modulus calculated by image analysis under triaxial compression with and without end lubrication: (a) Over whole *H*, (b) Over middle *H*/3. Front-Rear averages are shown for monotonic loading, and four-face averages for 2nd and 3rd cycles.

CONCLUSIONS

This study proposed an image analysis-based strain-measurement system in triaxial testing adopting stereophotogrammetry. What puts this study apart from previous developments with

stereophotogrammetry in soil laboratory is the effort to capture small displacements and strains to order of 10^{-3}mm and 10^{-3}%, with only middle-grade compact digital cameras. This was achieved by combination of Particle Tracking Velocimetry (PTV) and sub-pixel Digital Image Correlation (DIC), which firstly estimates approximate (although quite accurate even at this stage) coordinates of target points by fast binarisation and blob-detection processing, and then determines precise sub-pixel coordinates by pattern matching back in original greyscale. The ray tracing technique was adopted to correct for the view distortion due to the pressure cell wall and water. With two cameras at fixed positions, the accuracy for the relative displacements is within 1% of 5mm span. After averaging, the precision for the relative displacement was 0.002mm for the two camera's overall perspective direction, and 0.001mm for the perpendicular directions.

The proposed measurement method was adopted to characterise deformation of reconstituted clay samples in triaxial compression. Two tests were performed, with and without end lubrication. Strain distributions were visualised at each of small-strain loading/unloading cycles, consolidation and swelling, and eventual monotonic undrained loading to large strains. For 0.05% axial strain, undrained Poisson's ratio for the overall specimen was measured between 0.418-0.595, which fairly compares with the ideal value of 0.5. The trends for the secant undrained Young's modulus – axial strain curves, or 'stiffness degradation curves', were obtained for wide strain ranges, from around 0.005% axial strain up to 15%. While this is not yet as precise as conventional local displacement sensors such as LVDTs, the proposed method has many advantages, including wide measurable strain ranges, (semi-)full-field views, and the very limited hardware it requires. It is worth noting that the system without jigs and cables for local sensors inside the cell is highly comfortable to work with. Both in terms of the accuracy/precision and convenience, the proposed method based on stereophotogrammetry is practical as well as offering more research opportunities in laboratory soil characterisation.

ACKNOWLEDGMENTS

This study was conducted with JSPS KAKENHI Grant-in-Aid (19H02230).

REFERENCES

Ackerley, S. K., Standing, J. R. and Hosseini Kamal, R. (2016) A system for measuring local radial strains in triaxial apparatus. *Géotechnique* 66 (6) 515-522. DOI: 10.1680/jgeot.15.T.027

Bhandari, A. R., Powrie, W. and Harkness, R. M. (2011) A digital image-based deformation measurement system for triaxial tests. *Geotechnical Testing Journal* 35 (2) 209-226. DOI: 10.1520/GTJ103821

Bishop, A. W. and Green, G. E. (1965) The influence of end restraint on the compression strength of a cohesionless soil. *Géotechnique* 15 (3) 243-266. DOI: 10.1680/geot.1965.15.3.243

Butterfield, R., Harkness, R. M., Andrawes, K. Z. (1970) A stereo-photogrammetric method for measuring displacement fields. *Géotechnique* 20 (3) 308-314. DOI: 10.1680/geot.1970.20.3.308

CG-ARTS (2015): Digital image processing. Computer Graphic Arts Society, ISBN-13: 978-4903474502. 444p. (in Japanese)

Clayton, C. R. I. and Katrush, S. A. (1986) A new device for measuring local axial strains on triaxial

specimens. *Géotechnique* 36 (4) 593-597. DOI: 10.1680/geot.1986.36.4.593

Cuccovillo, T. and Coop, M.R. (1997) The measurement of local axial strains in triaxial tests using LVDTs. *Géotechnique* 47 (1) 167-171. DOI: 10.1680/geot.1997.47.1.167

Cui, W., Potts, D. W., Pedro, A. M. G. and Zdravković, L. (2020) No AccessNumerical assessment of the effects of end-restraints and a pre-existing fissure on the interpretation of triaxial tests on stiff clays. *Géotechnique* Ahead of Print. DOI: 10.1680/jgeot.19.P.318

Desrues, J. and Viggiani, G. (2004) Strain localization in sand: and overview of the experimental results obtained in Grenoble using stereophotogrammetry. *International Journal for Numerical and Analytical Methods in Geomechanics* 28 279-321. DOI: 10.1002/nag.338

Gachet, P., Geiser, F., Laloui, L. and Vulliet, L. (2007) Automated digital image processing for volume change measurement in triaxial cells. *ASTM Geotechnical Testing Journal* 30 (2) 98-103. DOI: 10.1520/GTJ100309

Germaine, J. T. and Ladd, C. C. (1988) Triaxial testing of saturated cohesive soils. *Advanced Triaxial Testing of Soil and Rock ASTM STP 977 (eds. Donaghe, R. T., Chaney, R. C. and Silver, M. L.)* ASTM, Philadelphia, USA, 421-459.

Goto, S., Tatuoka, F., Shibuya, S. Kim, Y.-S. and Sato, T. (1991) A simple gauge for local small strain measurements in the laboratory. *Soils and Foundations* 31 (1) 136-180. DOI: 10.3208/sandf1972.31.169

Jardine, R. J. (1992) Some observations on the kinematic nature of soil stiffness. *Soils and Foundations* 32 (2) 111-124. DOI: 10.3208/sandf1972.32.2_111

Kaehler, A. and Bradski, G. (2017) Learning OpenCV 3. O'Reilly, ISBN-13: 978-1-491-93799-0

Li, L., Zhang, X., Chen, G. and Lytton, R. (2016) Measuring unsaturated soils deformation during triaxial testing using a photogrammetry-based method. *Canadian Geotechnical Journal* 53 (3) 472-489. DOI: 10.1139/cgj-2015-0038

Li, L. and Zhang, X. (2018) Factors influencing the accuracy of the photogrammetry-based method. *Acta Geotechnica* 14 559-574 DOI: 10.1007/s11440-018-0663-4

Lin, H. and Penumadu, D. (2006) Strain localization in combined axial-torsional testing on kaolin clay. *ASCE Journal of Engineering Mechanics* 132 (5) 555-564. DOI: 10.1061/(ASCE)0733-9399(2006)132:5(555)

Liu, T. (2018) Advanced laboratory testing for offshore pile foundations under monotonic and cyclic loading, PhD thesis, Imperial College London, UK.

Nishimura, S. (2014a) Assessment of anisotropic elastic parameters of saturated clay measured in triaxial apparatus: Appraisal of techniques and derivation procedures. *Soils and Foundations* 54 (3) 364-376. DOI: 10.1016/j.sandf.2014.04.006

Nishimura, S. (2014b) Cross-anisotropic deformation characteristics of natural sedimentary clays. *Géotechnique* 64 (12) 981-996. DOI: 10.1680/geot.14.P.088

Nishimura, S., Iwaki, A., Takashino, S. and Tanaka, H. (2016) Image-based measurement of one-dimensional compressibility in cement-treated soils. *Géotechnique* 66 (10) 840-853. DOI: 10.1680/jgeot.15.P.218

OpenCV: Camera Calibration and 3D Reconstruction: https://docs.opencv.org/master/d9/db7/

tutorial_py_table_of_contents_calib3d.html (accessed on 19 April 2021)

Qiao, H., Nakata, Y., Hyodo. M. and Kikkawa, N. (2008) Triaxial compression test for unsaturated sandy soil using image processing technique. *The 4th International Symposium on Deformation Characteristics of Geomaterials, Atlanta (eds S. E. Burns, P. W. Mayne and J. C. Santamarina)*, 529-534. Amsterdam, the Netherlands: IOS Press.

Raffel, M., Willert, C. E., Wereley, S. and Kompenhans, J. (2007) Particle Image Velocimetry; A practical guide. Springer, ISBN 978-3-540-72308-0

Rattez, H., Shi, Y., Sac-Morane, A., Klaeyle, T., Mielniczuk, B. and Veveakis, M. (2021) Effect of grain size distribution on the shear band thickness evolution in sand. *Géotechnique* Ahead of Print. DOI: 10.1680/jgeot.20.P.120

Timoshenko, S. P. and Goodier, J. N. (1970) Theory of elasticity. Third edition, McGraw-Hill, New York, ISBN-13: 978-0070701229

Vardanega, P. J. and Bolton, M. D. (2013) Stiffness of clays and silts: Normalizing shear modulus and shear strain. *ASCE Journal of Geotechnical and Geoenvironmental Engineering* 139 (9) 1575-1589. DOI: 10.1061/(ASCE)GT.1943-5606.0000887

Vinck, K., Liu, T., Ushev, E. and Jardine, R. J. (2019) An appraisal of end conditions in advanced monotonic and cyclic triaxial testing on a range of geomaterials. *7th International Symposium on Deformation Characteristics of Geomaterials (eds. Tarantino, A. and Ibraim, E.)*, Glasgow, DOI: 10.1051/e3sconf/20199202007

Vucetic, M. and Dobry, R. (1991) Effect of soil plasticity on cyclic response. *ASCE Journal of Geotechnical Engineering* 117 (1) 89-107. DOI: 10.1061/(ASCE)0733-9410(1991)117:1(89)

White, D. J., Take, W. A. and Bolton, M. D. (2003) Soil deformation measurement using particle image velocimetry (PIV) and photogrammetry. *Géotechnique* 53 (7) 619–631, DOI: 10.1680/geot.2003.53.7.619

Zhang, X., Li, L., Chen, G. and Lytton, R. (2014) A photogrammetry-based method to measure total and local volume changes of unsaturated soils during triaxial testing. *Acta Geotechnica* 10 55–82. DOI: 10.1007/s11440-014-0346-8

Zhang, X., Li, L. and Xia, X. (2019) Recent advances in volume measurements of soil specimen during triaxial testing. 7th Asia-Pacific Conference on Unsaturated Soils, JGS Special Publication 7 (2) 31-37. DOI: 10.3208/jgssp.v07.004

Zhao, C., Koseki, J. and Liu, W. (2020) Local deformation behaviour of saturated silica sand during undrained cyclic torsional shear tests using image analysis. *Géotechnique* 70 (7) 621-629. DOI: 10.1680/jgeot.18.T.017

LIST OF NOTATIONS

Superscripts *L* and *R* are added to some of these to indicate left and right cameras, respectively.

A: Matrix relating *X*-*Y*-*Z* to *u*-*v*

$E_{u,sec}$: Secant undrained Young's modulus

f: Focal distance of camera

H: Specimen height

$\mathbf{i_0}$, $\mathbf{i_1}$, $\mathbf{i_2}$: Ray tracing vectors

n_a, n_c, n_w: Absolute refraction indices for air, cell (acrylic) wall and water, respectively

p': Mean effective stress

P: Perspective projection matrix

p_{ij}: Elements of **P**

r: $=\sqrt{f(X/Z)^2+f(Y/Z)^2}$

R: Rotation matrix of X_w-Y_w-Z_w to *X*-*Y*-*Z*

t: Translation vector of X_w-Y_w-Z_w to *X*-*Y*-*Z*

u, *v*: Image space coordinates

u_0, v_0: Ray axis offsets from the image centre

X, *Y*, *Z*: Camera coordinates

X_w, Y_w, Z_w: Real physical world coordinates

X_{w2}, Y_{w2}, Z_{w2}: Origin of vector $\mathbf{i_2}$

γ_{ar}: Shear strain in axial-radial plane

δ_u, δ_v: Physical spacings between each light-sensing pixel in the *u* and *v* directions

ε_a, ε_r, ε_θ, ε_v: Axial, radial, circumferential and volumetric strains

$\dot{\varepsilon}_a$: Axial strain rate

η: A scalar

λ: A scalar

ν_u: Undrained Poisson's ratio

σ: Standard deviation (of displacement)

σ_{vc}': Vertical effective stress at preconsolidation